Electrical Power and Energy Systems 142 (2022) 108305

Contents lists available at ScienceDirect

International Journal of Electrical Power and Energy Systems

journal homepage: www.elsevier.com/locate/ijepes

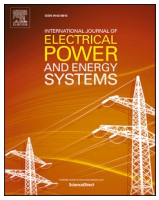

Integration of air-cooled multi-stack polymer electrolyte fuel cell systems into renewable microgrids

J.M. Andújar [a], F.J. Vivas [a,*], F. Segura [a], A.J. Calderón [b]

[a] University of Huelva, CITES (Centro de Investigación en Tecnología, Energía y Sostenibilidad), Campus El Carmen, 21071 Huelva, Spain
[b] University of Extremadura, Department of Electrical, Electronics Engineering and Automatic, Campus Universitario, Av. de Elvas, s/n, 06006 Badajoz, Spain

ARTICLE INFO

Keywords:
Renewable-based microgrid
High-voltage DC bus
Air-cooled PE fuel cell
Multi-stack architecture
Isolated power converter
Virtual instrument
Real time control and monitoring

ABSTRACT

Currently, there is a growing interest in increasing the power range of air-cooled fuel cells (ACFCs), as they are cheaper, easier to use and maintain than water-cooled fuel cells (WCFCs). However, air-cooled stacks are only available up to medium power (<10 kW). Therefore, a good solution may be the development of ACFCs consisting of several stacks until the required power output is reached. This is the concept of air-cooled multi-stack fuel cell (AC-MSFC). The objective of this work is to develop a turnkey solution for the integration of AC-MSFCs in renewable microgrids, specifically those with high-voltage DC (HVDC) bus. This is challenging because the AC-MSFCs must operate in the microgrid as a single ACFC with adjustable power, depending on the number of stacks in operation. To achieve this, the necessary power converter (ACFCs operate at low voltages, so high conversion rates are required) and control loops must be developed. Unlike most designs in the literature, the proposed solution is compact, forming a system (AC-MSFCS) with a single input (hydrogen) and a single output (high voltage regulated power or voltage) that can be easily integrated into any microgrid and easily scalable depending on the power required. The developed AC-MSFCS integrates stacks, balance of plant, data acquisition and instrumentation, power converters and local controllers. In addition, a virtual instrument (VI) has been developed which, connected to the energy management system (EMS) of the microgrid, allows monitoring of the entire AC-MSFCS (operating temperature, purging, cell voltage monitoring for degradation evaluation, stacks operating point control and alarm and event management), as well as serving as a user interface. This allows the EMS to know the degradation of each stack and to carry out energy distribution strategies or specific maintenance actions, which improves efficiency, lifespan and, of course, saves costs. The experimental results have been excellent in terms of the correct operation of the developed AC-MSFCS. Likewise, the accumulated degradation of the stacks was quantified, showing cells with a degradation of >80%. The excellent electrical and thermal performance of the developed power converter was also validated, which allowed the correct and efficient supply of regulated power (average efficiency above 90%) to the HVDC bus, according to the power setpoint defined by the EMS of the microgrid.

1. Introduction

In the last decade, the efforts made by countries to reach a major agreement on climate change, which materialised at the recent COP25 (25th conference of the parties), have been particularly noteworthy [1]. As a result of this agreement, there are great expectations and investments for the total migration of the current energy system to a more sustainable one based on the use of renewable energy sources. In this new energy model, microgrids will play a pivotal role [2]. In this framework, hydrogen is set to be the energy vector of the near future for stationary and mobile applications [3,4]. The use of hydrogen as an energy vector has been successfully tested in microgrids with different renewable generation and consumption profiles [5,6].

Despite the multiple benefits of hydrogen technologies, the still reduced lifespan of electrolysers and, specially, of FCs, coupled to their high current cost (although it has been considerably reduced in recent years), requires a great effort in research and technology, so that hydrogen technologies are seen by governments, companies and society in general as a true substitute for the current fossil fuel-based economy [7].

* Corresponding author.
E-mail address: francisco.vivas@diesia.uhu.es (F.J. Vivas).

https://doi.org/10.1016/j.ijepes.2022.108305
Received 21 March 2022; Received in revised form 25 April 2022; Accepted 2 May 2022
Available online 11 May 2022

Nomenclature

List of acronyms

AC	alternating current
ACFC	air-cooled fuel cell
AC-MSFC	air-cooled multi stack fuel cell
AC-MSFCS	air-cooled multi stack fuel cell system
ADC	analog-to-digital converter
AI	analog input
AO	analog output
AP	area product
BoL	beginning of the lifespan
BoP	balance of plant
CLSMS	cell-level stack monitoring system
CU	control unit
DC	direct current
DO	digital output
EMI	electromagnetic interference
EMS	energy management system
ESS	energy storage system
FC	fuel cell
ICS	instrumentation and control system
MSFC	multi-stack fuel cell
MSFCS	multi-stack fuel cell system
NTC	negative temperature coefficient
PE	polymer electrolyte
PE-FC	polymer electrolyte fuel cell
PID	proportional–integral–derivative
PWM	pulse width modulation
RFI	radio frequency interference
SCADA	supervisory control and data acquisition
UI	user interface
VI	virtual instrument

Notation and symbols

A_E	core magnetic cross-section area (cm^2)
AP	core area product (cm^4)
A_W	window area available for the winding (cm^2)
B	fuel cell type dependent parameter for concentration overvoltage calculation (V)
β	NTC Beta Parameter
C	parameter associated with the converter topology (0.017 in this case)
C_o	output low-pass filter capacitor (F)
C_{O_2}	oxygen concentration between the cathode and the catalytic layer (mol/cm^3)
δ	duty cycle
ΔB	flux density deviation swing (Tesla, T)
$\Delta I_{L_s}(t)$	output low-pass filter inductor ripple current (A)
ΔG	change of free Gibbs energy of the electrochemical reaction (J/mol)
ΔS	change of entropy of the electrochemical reaction (J/mol)
$\Delta V_{C_O}(t)$	output low-pass filter capacitor ripple voltage (V)
F	Faraday constant (96485 C/mol)
φ	adjustable parameter for membrane resistivity calculation
f_T	transformer operating frequency (Hz)
$I_{C_o}(t)$	output low-pass filter capacitor current (A)
$I_{FC}(t)$	stack current = fuel cell current = cell current (A)
$I_{L_s}(t)$	output low-pass filter inductor current (A)
I_{Max}	maximum stack current = maximum cell current (A)
I_o(t)	output current (A)
l	membrane thickness (cm)
L_s	output low-pass filter inductor (H)
N_{FC}	number of cells in the stack
N_p	number of turns of transformer primary winding
N_s	number of turns of transformer secondary winding
P_{Down}	fuel cell power for the downward operation (W)
P_{FC}	fuel cell power (W)
P_{H_2}	partial pressure of hydrogen (atm)
P_{O_2}	partial pressure of oxygen (atm)
P_o	power output (W)
P_{Ref}	fuel cell power setpoint (W)
P_{Teo}	fuel cell power at the beginning of life (W)
P_{Up}	fuel cell power for the upward operation (W)
R	universal gas constant (8.31 J K^{-1} mol^{-1})
R_C	electrodes resistance (Ω)
R_L	load resistor (Ω)
R_M	membrane resistance (cm^2)
ρ_M	Membrane resistivity (Ω cm)
T_{FC}	fuel cell stack temperature (°C)
Đ¤	magnetic flux intensity (Wb)
T_{Max}	fuel cell stack maximum temperature (°C)
T_{Min}	fuel cell stack minimum temperature (°C)
T_{Opt}	optimum fuel cell stack temperature (°C)
T_{FC}	fuel cell stack temperature (°C)
V	voltage induced in a transformer turn (V)
V_{act}	activation overpotential (V)
V_{con}	concentration overpotential (V)
$V_{C_O}(t)$	output low-pass filter capacitor voltage (V)
V_{Down}	fuel cell voltage for the downward operation (V)
V_{FC}	fuel cell output voltage (V)
$V_{L_s}(t)$	inductor voltage (V)
V_{Nernst}	Nernst voltage (V)
V_o	output voltage (V)
V_{ohm}	voltage drop due to ohmic loses (V)
V_{ref}	reference output voltage (V)
V_s	transformer secondary voltage (V)
V_{Teo}	fuel cell voltage at the beginning of life (V)
V_{Up}	fuel cell voltage for the upward operation (V)
ξ_1	Cell type dependent parameters (V)
$\xi_2 - \xi_4$	Cell type dependent parameters (V/K)

1.1. Problem statement and state of art

Considering microgrids with hydrogen as energy vector, topologies based on HVDC bus have recently proliferated [8–10]. Indeed, topologies whose DC bus is supported by batteries present advantages in terms of simplicity in voltage control [2,9]. This architecture makes it possible to reduce losses, as well as to avoid problems related to power factor, reactive power, or power quality [2,11]. In the same way, DC bus-based microgrids facilitates the integration of DC generation systems and DC loads, such as photovoltaic panels, batteries, FCs, electrolysers, etc.

Regarding FCs, the polymer electrolyte (PE) type is the most widespread due to its low operating temperature, fast response and high efficiency [12,13]. Depending on the power rating, the commercial solutions are based on the use of ACFCs (<10 kW) or WCFCs (>10 kW). ACFCs have more advantages in terms of operation and design than WCFCs. These include simpler balance of plant (BoP) and associated control [12,13]. However, its maximum operating power, limit its use in practical applications such as microgrids. The use of AC-MSFCs solve this problem, increasing efficiency and reliability due to their redundancy [13,14].

However, to properly integrate AC-MSFCs into a HVDC bus-based

microgrid, a suitable BoP is required, to ensure correct stoichiometry and thermal management [15]; a high conversion ratio power converter, to ensure integration into high-voltage DC bus [16]; and control and instrumentation units, to monitor and manage the entire operation of the AC-MSFC [17,18]. All these elements working together in a controlled manner constitute the AC-MSFCS.

It is essential to highlight the need to monitor the degradation of each cell of each AC-MSFCS stack, to quantify the accumulated degradation and identify cause-effect relationships to mitigate the negative effects on the lifespan of the system determined by its operating conditions (temperature, voltage and current) [19]. If this is not known and regulated, the advantages offered by the multi-stack concept will be drastically diminished, as there will be a power imbalance in the stacks lines, since the degradation of the stacks is neither uniform (analogous in all their cells) nor even (equal in all stacks).

Considering the above, the use of AC-MSFCSs requires a considerable effort in the design of auxiliary equipment to ensure its operation, which will considerably increase the number of parameters, control loops and information that the EMS must handle, and ultimately, this will result in an increase in the complexity of its design and implementation. To avoid this, the use of comprehensive solutions that allow the highest level of abstraction in the management and control of AC-MSFCSs by the EMS is crucial.

Regarding the proposed solutions for the integration of AC-MSFCSs in microgrids, some configurations use parallel topology to increase redundancy and system efficiency, or series topology to increase the overall voltage and reduce complexity in the design of the power conversion stage. A simple solution is presented in [20], where the design of a AC-MSFCS with series topology of ACFCs for use in small applications and power up to 50 kW is evaluated. This topology facilitates integration through the use of non-isolated boost converters, but reduces system performance and does not guarantee correct operation in case of high stacks degradation. In [21], the proposal is based on the serialisation of stacks and the use of bypass diodes and switches in parallel, with the aim of isolating the stack that presents a high degradation. As in the previous case, the efficiency of the serial topology was determined by the poorest stack.

On the other hand, [22] presents a modular system with parallel architecture based on WCFCs and a boost converter topology with power up to 100 kW. A similar topology is used in [14,23], where several stacks are parallelised to obtain a high-power propulsion system for an electric vehicle application. The use of these topologies makes it possible to ensure system redundancy and increase the overall efficiency at the expense of a greater number of elements and an increase in the complexity of the control system. With the aim of reducing the number of power converters, a parallel topology based on AC-MSFCS for hybrid microgrids is presented in [24]. This architecture is based on the use of a single non-isolated boost converter connected to the output of the AC-MSFC. An improved solution is presented in [25], where the use of a parallel architecture of AC-FCs, and the serialisation of non-isolated boost power converters at their output is evaluated. The proposed architecture allows achieving the required voltage conversion ratio for AC-MSFCS integration using simpler topologies. Finally, in [26] a hybrid series–parallel architecture solution is presented with the aim of increasing the performance of the AC-MSFCS. This topology is based on the serialisation of stacks to achieve a higher operating voltage, and the parallelisation of series of stacks, with the aim of increasing the current and redundancy of the AC-MSFCS.

Regardless of the AC-MSFCS architecture, the most common solutions are based on non-isolated power converters, mainly interleaved boost topologies [14,20,24–26]. But this present a limitation in terms of safety, due to the lack of insulation between the FC system and the DC bus, as well as of the maximum effective conversion ratio [27]. To solve these problems, the use of isolated power converters is employed. In low power applications, the use of Flyback type topologies is widespread, due to their simplicity and reduced number of components [28,29]. But for medium and high-power applications, solutions based on push–pull [30,31] and full bridge converters [32,33] are used to guarantee high efficiencies.

In any case and regardless of the above, something that conditions the power conditioning stage is that AC-FCs operate at low voltage, so the use of power converters with a large conversion ratio is required to ensure their correct integration on HVDC buses [34,35].

On the other hand, regarding instrumentation/control solutions for AC-MSFCS, the vast majority are oriented to a low-level local control to guarantee the correct operation of the BoP, but not to provide a data acquisition system that allows real-time control and monitoring of the operation and degradation of the stacks in real applications. Thus, a simple solution is developed in [36], where the developed software tool (virtual instrument, VI) allows the monitoring and control of parameters of a reduced BoP associated to a small PE FC for educational purposes. The developed VI does not include specific solutions for alarm detection and management, as well as the integration of power electronics. On the other hand, a proposal for an alarm management system is developed in [37], where a VI for monitoring BoP parameters of a FC is developed. A more powerful and complete solution is presented in [38], where a VI for monitoring and controlling the BoP of a WCFC is developed. Finally, the work published in [17] proposes the design of a VI which has the dual function of acting as a BoP simulator, as well as a SCADA (supervisory control and data acquisition) system in real applications. Despite its advantages, this solution ignores the integration of the power conditioning stage, necessary to guarantee the integration of the FC system into the microgrid.

As a conclusion of the review of the scientific literature carried out, there is a lack of comprehensive solutions (only partial solutions are presented) to the problem of integration, control and management through a VI (or similar) of the AC-MSFCS, which allows easy and complete integration, control, degradation quantification and monitoring of the AC-MSFCS or WC-MSFCS in the microgrid, and with the necessary level of abstraction to allow an easy handling by any EMS.

2. Aims and contributions

This paper presents a comprehensive answer to the problem of connecting and operating AC-MSFCSs in high-voltage DC bus microgrids powered by renewable energy sources.

For practical microgrids interconnected with distribution grids, it is essential to achieve the best DC/AC coupling. This implies the use of HVDC buses, since it allows working with high power at low currents. In this sense, to couple unregulated low-voltage sources, such as FCs, to a HVDC buses, one solution could be to use a high-power FC, which ensures a higher output voltage. However, this has three major problems: (1) It may not be necessary to have so much power permanently, which would mean continuously shutting down/starting up the FC. This has the disadvantage of shortening its lifespan and increasing the operating cost of the microgrid. (2) A failure in the FC means leaving the microgrid without hydrogen support. And (3), The power steps involved in the operation or shutdown of the FC provide a reduced degree of freedom to the controller to establish intermediate powers. Based on this analysis, the solution proposed in this work is to provide hydrogen support to the microgrid through different stacks, individually operable, within the set called AC-MSFCS. For this purpose, a high performance DC/DC converter has been developed, which can be cloned as many times as stacks lines are needed (as many as the AC_MSFCS has), and which is specifically designed to allow coupling between very different voltage levels (stack output and HVDC bus).

In addition to the above, to increase the performance and lifetime of the AC-MSFCS, the development of an internal management system that informs the microgrid EMS is required to activate only the number of stacks needed to guarantee the load demand, thus preserving the unnecessary deterioration of the remaining stacks [13]. Moreover, since the EMS has information about the degradation of the AC-MSFCS stacks,

it can selectively turn on each of stack line to obtain the same degree of degradation in all of them (preventive maintenance). Even, as cell-level information [19] is available within each stack, the degradation of each cell can be known in advance, which allows acting before degradation of adjacent cells occurs [39]. In other words, it is possible to determine the state of the cells in each stack to estimate when maintenance should be carried out, i.e., predictive maintenance is performed. The cell-level stack monitoring system (CLSMS) has been patented by the authors [40].

After a careful review of the literature, no proposals for practical systems with the characteristics and performance of those presented in this paper have been found.

As mentioned above, the lack of practical solutions to the problem posed has been precisely the motivation for this research. Thus, its main contribution lies in the design of a compact system that integrates the entire AC-MSFCS solution in a single set: multi-stacks architecture, BoPs, signals conditioning, acquisition electronics, CLSMS, real-time monitoring, power converter, local controllers, and communications layer necessary for the correct management of the MSFCS and its easy interconnection with EMS. To address this objective, and minimize the design tasks and the parameters to be controlled by the EMS, the proposed design concept has focused on presenting the AC-MSFCS as a compact set with a single input (hydrogen) and a single output (regulated power or voltage). In addition, the AC-MSFCS provides the EMS with all the necessary information to provide sufficient degrees of freedom to enable the implementation of advanced energy management strategies in the microgrid.

According to the application and to provide the system with maximum versatility, two control loops have been developed, voltage control and power control, both selectable by the EMS. The voltage control will allow the EMS to address the DC bus voltage regulation problem in conjunction with the other local controllers, as well as to implement controlled charging protocols if the DC bus is supported by a direct connection of a battery bank. On the other hand, the power control can be used by the EMS to impose to each stack a different operating power different than the nominal one, allowing advanced strategies oriented to increase the performance and lifespan of the AC-MSFCSs, making a uniform use of its stacks according to their accumulated degradation. Finally, this work also presents the development of a VI that allows the monitoring and control of the entire AC-MSFCS, as well as serving as an ergonomic user interface. Of course, the design methodology facilitates its extrapolation to any other AC-MSFCS, since it is only a scaling problem depending on the power and number of stacks in the system. The concept of reconfigurable MSFCS has been patented by the authors [41].

Table 1 shows the novelty of this work, highlighting its main contributions with respect to the literature analysed.

The paper is organized as follows, Section 2 describes materials and methods, fuel cell and converter model, as well as all the facilities, devices and software tools specially designed to carry out the research. Section 3 presents the experimental validation of the developed AC-MSFCS and discussion of its results. Finally, in Section 4 the main conclusions of the research are addressed.

3. Materials and methods

The developments presented in this paper refer to the actions required for the integration of an AC-MSFCS into a HVDC renewable microgrid, specifically in the one presented in Fig. 1. This microgrid is part of the facilities of the research group to which the authors of this work belong. The DC bus of the microgrid is a high-voltage bus and, although its nominal value is 360 V, depending on the state of charge of the battery bank (as it can be seen directly connected to the bus), it can vary from 340 to 420 V. Both are, respectively, the limits that set the minimum and maximum state of charge to preserve the best lifespan of the battery bank. As for the rest of the elements of the microgrid, they will not be described because they are not the subject of this research.

The starting point in the design and implementation of the AC-MSFCS is the stack to be used and the number of units. In this case, the chosen PE stack model was the Ballard® FCgen-1200ACS (Fig. 2(a)) with a rated power of 3.4 kW. In practice, this power is already difficult to achieve in brand new FCs, and even more so in used ones [13,42], as in the case of this research. As is well known, stacks deteriorate with use and for different reasons (even for storage time from manufacture to use) [43,44].

In this application, the number of FC units has been set at 3, just the number available, to form an AC-MSFCS of 10.2 kW rated power. From this first decision, the steps to follow to reach the final AC-MSFCS are the design and implementation of: BoP of each stack, DC/DC power converter and control unit (CU) of each stack and, finally, a VI which oversees data acquisition, variable monitoring and shutdown/startup of the entire system. The supervisory control of the AC-MSFCS is carried out by the EMS of the microgrid (it is already available and is therefore not the subject of this research although it will be necessary to include the AC-MSFCS signals and reprogram it); however, the correct operation of the AC-MSFCS is the task of its local controllers, as will be seen in this section. Fig. 2(b) shows the AC-MSFCS to be implemented. CU will be explained in section 2.4. The proposed design can be multiplied according to the number of stacks and easily adapted to the rated operating power/voltage according to the system architecture shown in Fig. 2 (b). In the following sections each of the developed subsystems will be described.

Table 1
Contributions of the proposed work with respect to previous scientific works analysed.

Reference	MSFC topology	BoP integration	Power conditioner	ICS&UI*	CLSMS	Integral solution
[36–38]	Single-stack	Yes	No	Yes	No	No
[17]	MSFC. Parallel	Yes	No	Yes	No	No
[28,29]	Single-stack	No	Isolated flyback converter	No	No	No
[30,31]	Single-stack	No	Isolated push–pull converter	No	No	No
[32,33]	Single-stack	No	Isolated full bridge converter	No	No	No
[20]	MSFC. Series	No	Non-isolated unique boost converter	No	No	No
[21]	MSFC Series and bypass diode	No	Non-isolated unique boost converter	No	No	No
[14,22,23]	MSFC. Parallel	No	Non-isolated parallelised boost converter	No	No	No
[24]	MSFC. Parallel	No	Non-isolated unique boost converter	No	No	No
[25]	MSFC. Parallel	No	Non-isolated serialised boost converter	No	No	No
[26]	MSFC Hybrid topology	No	Non-isolated parallelised boost converter	No	No	No
Authors proposal	MSFC. Parallel	Yes	Isolated parallelised push–pull converter	Yes	Yes	Yes

* Instrumentation and control system with user interface (usually a VI)

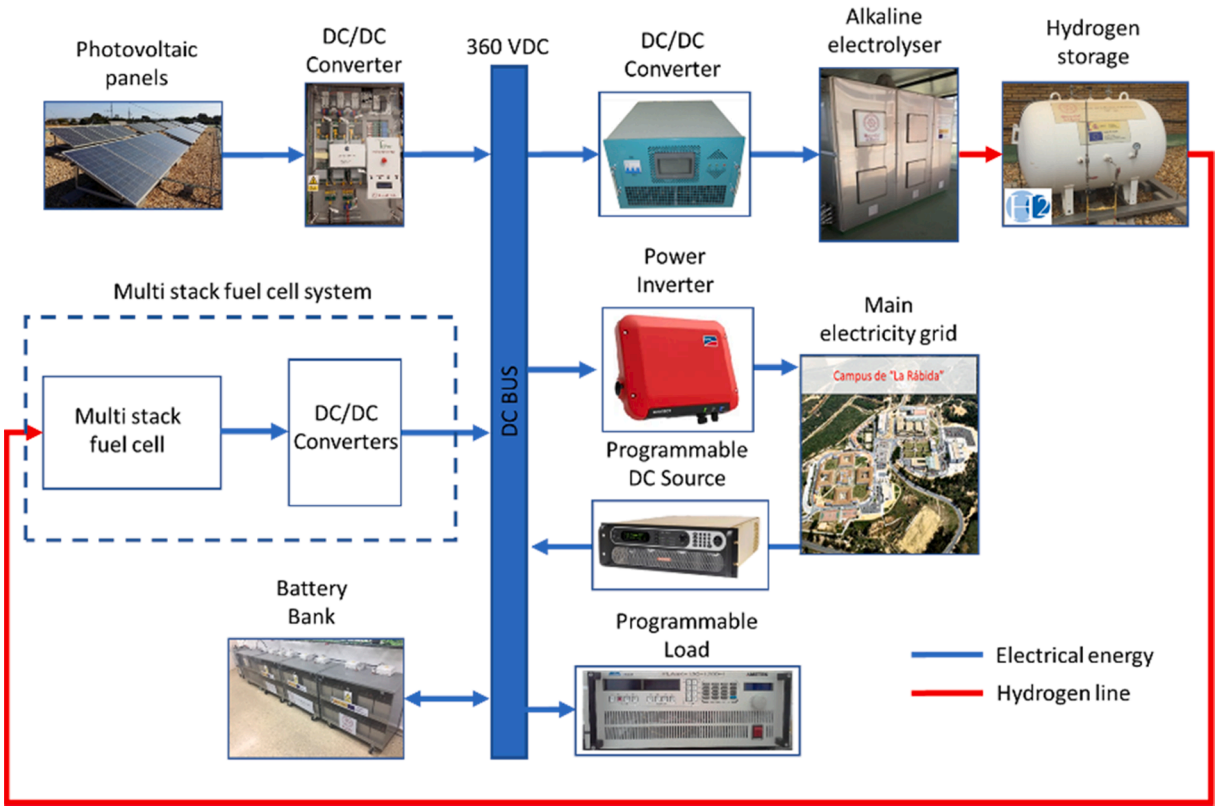

Fig. 1. General renewable microgrid architecture. In dashed line the topic of this research.

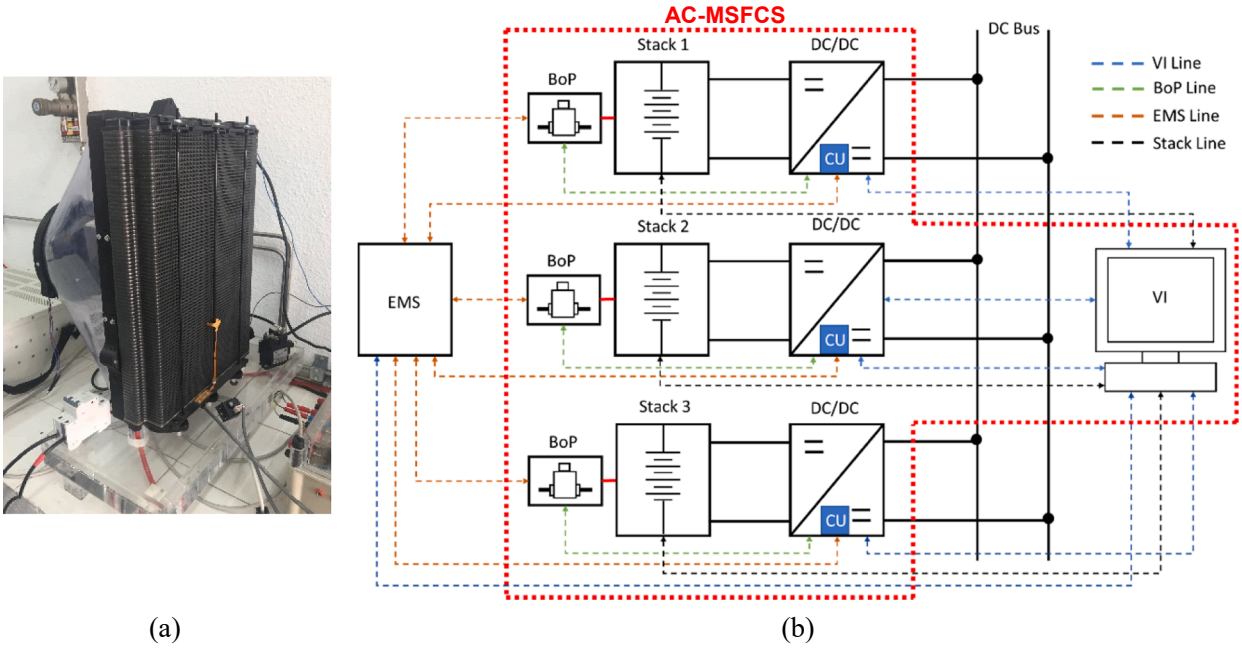

Fig. 2. (a) Ballard® model FCgen-1200ACS stack; (b) MSFCS architecture.

3.1. Fuel cell

The stack of a FC is an electrochemical device, composed of several cells in series, N_{FC}, in which the reaction of hydrogen and oxygen gas produces water, electrical energy and heat as by-products. The steady-state voltage generated between the stack terminals is defined by equation (1) [5,45].

$$V_{FC} = N_{FC}(V_{Nernst} - V_{act} - V_{ohm} - V_{con}) \quad (1).$$

The meaning of each term in (1) is as follows. V_{Nernst} models the potential difference that exists at the reaction equilibrium for given conditions of temperature and partial pressures of the reactants, and is given by equation (2) [5,45].

$$V_{Nernst} = \frac{\Delta G}{2F} + \frac{\Delta S}{2F}(T_C - T_{ref}) + \frac{RT_C}{2F}\left(\ln\left(P_{H_2} + \frac{1}{2}P_{O_2}\right)\right) \quad (2).$$

Where:

ΔG: Change of free Gibbs energy of the electrochemical reaction ($J \cdot mol^{-1}$).

ΔS: Change of entropy of the electrochemical reaction ($J \cdot mol^{-1}$).

R: universal gas constant (8.31 $J \cdot K^{-1} \cdot mol^{-1}$).

F: Faraday constant (96485$C \cdot mol^{-1}$).

P_{H_2}: Partial pressure of hydrogen (atm).

P_{O_2}: Partial pressure of oxygen (atm).

T_C: Cell operating temperature (K).

T_{ref}: Reference temperature (K).

V_{act} represents the losses associated with reaction activation, which is strongly related to temperature, oxygen partial pressure and cell current according to equation (3) [45,46].

$$V_{act} = -(\xi_1 + \xi_2 T_{FC} + \xi_3 T_C ln(C_{O_2}) + \xi_4 T_c ln(I_{FC})) \quad (3).$$

Where:

ξ_1: Cell type dependent parameter (V).

$\xi_2 - \xi_4$: Cell type dependent parameters ($V\ K^{-1}$).

C_{O_2}: Oxygen concentration between the cathode and the catalytic layer ($mol \cdot cm^3$).

V_{ohm} determines voltage drops due to resistance in charge transfer across the electrodes and membrane. They are modeled as ohmic losses according to equation (4) [5,45].

$$V_{ohm} = I_{FC}(R_C + R_M) \quad (4).$$

Where:

R_C: Electrode resistance (Ω).

R_M: Membrane resistance (Ω).

The electrode resistance can be considered constant, while the membrane resistance has a strong relationship with the temperature and operating current of the cell, according to equations (5) and (6) [45,46].

$$R_M = \frac{\rho_M l}{A} \quad (5).$$

Where:

ρ_M: Membrane resistivity (Ω·cm).

l: Membrane thickness (cm).

A: Cell active area (cm^2).

$$\rho_M = \frac{181.6\left[1+0.03\left(\frac{I_{FC}}{A}\right)+0.062\left(\frac{T_C}{303}\right)^2\left(\frac{I_{FC}}{A}\right)^{2.5}\right]}{\left[\varphi-0.634-3\left(\frac{I_{FC}}{A}\right)\right]e^{4.18\left(T_C-\frac{303}{T_C}\right)}} \quad (6).$$

Where:

φ: Adjustable parameter with a maximum value of 23.

Finally, V_{con} models the voltage drop due to excess reactant concentration on the catalytic surfaces, and is determined by equation (7) [45,46].

$$V_{con} = -B \bullet ln\left(1 - \frac{I_{FC}}{I_{max}}\right) \quad (7).$$

Where:

B: Cell type dependent parameter (V).

I_{max}: Maximum cell current (A).

According to its manufacturing parameters, for the Ballard® stack model FCgen-1200ACS ($N_{FC} = 80$), equation (1) is written as a function of current as in (8) [43].

$$V_{FC} = 80\left(1005 - 39.9log(I_{FC}) - 3.44I_{FC} - 118e^{-0.021I_{FC}}\right)/1000 \quad (8).$$

3.2. Balance of plant design and implementation

The BoP of each stack is composed of all those pneumatic, mechanical, and electrical elements required to guarantee the correct operation of the stack in the optimum conditions of pressure, temperature and moisture for any power profile. In this case, the BoP is made up of three subsystems or lines (Fig. 3): hydrogen, air (cooling and stoichiometry) and electric.

The main characteristics of the elements that make up the BoP are listed in Table 2. In the specific case of the chosen stack, the simplicity of

Table 2
Main parameters of the BoP components.

Element	Model	Characteristics
Pressure sensor	8316, Burkert®	Supply voltage: 24 V Output signal: 4–20 mA Pressure range: 4 bar
Solenoid valve	6013, Burkert®	Supply voltage: 24 V Operating pressure: 10 bar
Hydrogen sensor	FCM6812, FIGARO®	Supply voltage: 5 VDC Output signal: 0–4.5 VDC Detection range: 0–14000 ppm
Temperature sensor	NTCS0603E3104JXT, Vishay®	Resistance (25 °C): 100 kΩ Temperature range: −40 … 150 °C β: 4100 K
Fan	DV 6224 TDA, Ebmpapst®	Supply voltage: 24 VDC Power: 91 W Air flow: 700 m^3/h
Diode	T110HF120, Vishay®	Maximum forward current: 110 A Maximum reverse voltage: 120 VDC
Safety relay	AEV14024, Panasoic®	Supply voltage: 16–36 VDC Current rating: 120 A Voltage switching capacity: 400 VDC

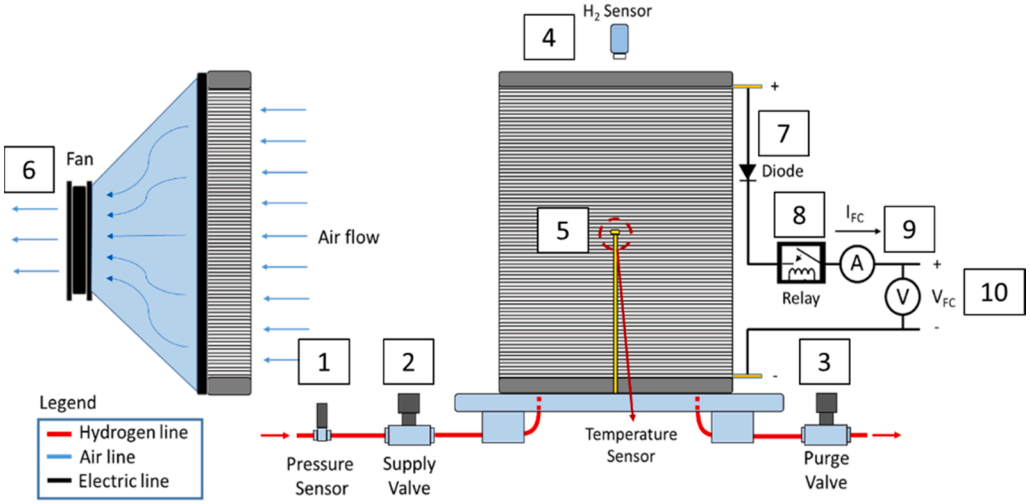

Fig. 3. Single Fuel Cell scheme (stack + BoP).

its BoP implies that it is not worth sharing elements among the three stacks. Thus, in what follows in this paper, the design and implementation of each of the FC lines of Fig. 2(b) is identical.

3.2.1. Hydrogen subsystem design

The hydrogen subsystem is responsible for ensuring the correct hydrogen supply to the stack, as well as the hydrogen purge according to the operating conditions.

For this purpose, the hydrogen supply line integrates a pressure sensor (1, Fig. 3) and a solenoid valve (2, Fig. 3), whose function is to allow and guarantee the supply of hydrogen pressure according to the requirements of the stack (1.16–1.69 bar). On the other hand, purging is carried out by means of another solenoid valve (3, Fig. 3). Its opening determines the free exit of pressurized hydrogen inside the stack and, therefore, the removal and elimination of impurities and excess water in each cell. The optimal purge interval is a trade-off between hydrogen consumption and stack lifespan. The recommended purge interval to increase the lifespan depends on the integration in time of the operating current, with the manufacturer recommending 3000 A.s. [43]. However, it can be modified according to the operating conditions or accumulated degradation of the stack. As for the purge time, 300 ms is considered enough to guarantee the correct purge process in the cells at rated current [43]. Finally, an electrochemical sensor is included to measure the hydrogen concentration in the environment (4, Fig. 3), in order to detect hydrogen leaks in any cell of the stack. This will trigger an alarm protocol with immediate shutdown for safety reasons: interruption of the hydrogen supply, opening of the purge valve, forced ventilation and electrical isolation of the stack.

The control of the supply and purge solenoid valves, as well as the measurement of hydrogen pressure and hydrogen concentration sensors are implemented by the CU located in the DC/DC converter (see section 2.4). The VI connects with this unit to monitor and show the evolution of the variables of interest (see Fig. 2(b)).

3.2.2. Air-cooling and stoichiometry subsystem design and implementation

The function of the oxidation/cooling subsystem is to provide the proper air supply to ensure the minimum stoichiometric ratio and optimum stack temperature, [47], based on the operating current, equation (9), according to the manufacturer's recommendations [43]. The operation at such temperature guarantees the stability of the cell and its optimum moisture point, which will also determine its optimum performance. Similarly, the manufacturer sets safe maximum and minimum continuous operating temperature limits that guarantee practically stable stack performance, equations (10) and (11) [43]. These limits will determine the alarm conditions of the stack, which will force a controlled shutdown of stack. Finally, the values of the constants used were calculated by the manufacturer from experimental tests, from the thermal model of the cell, as well as from the fundamental design and construction parameters of the bipolar plates [43].

$$T_{Opt}(t) = 0.53 \bullet I_{FC}(t) + 26.01 \quad (9)$$

$$T_{Max}(t) = 0.369 \bullet I_{FC}(t) + 52 \quad (10)$$

$$T_{Min}(t) = 0.57 \bullet I_{FC}(t) + 7 \quad (11)$$

Where:

$T_{Opt}(t)$: Optimum stack temperature (°C).

$T_{Max}(t)$: Maximum stack temperature (°C).

$T_{Min}(t)$: Minimum stack temperature (°C).

$I_{FC}(t)$: Stack or FC current (A).

An NTC-type thermistor (5, Fig. 3) is available for measuring the stack temperature ($T_{FC}(t)$). The control of the stack temperature is performing by the scheme of Fig. 4. The controller, a PID in this case, receives a temperature error signal from which it generates a control pulse that acts on a high-flow axial fan with speed regulated by PWM (Pulse Width Modulation). Thus, depending on the width of the control pulse, or duty cycle (δ), the fan is not powered ($\delta = 0$, air flow = 0 m^3/h) or it is powered all the time ($\delta = 1$, air flow = 700 m^3/h or 11666.66 slpm), with, obviously, all values in between. The fan is assembled in the outlet hole of a proprietary nozzle design to direct the airflow uniformly (6, Fig. 3), because it is essential that the temperature of the stack be uniform over its entire surface. To ensure the stoichiometry of the reaction, regardless of the temperature of the stack, a minimum air flow rate of 30% of the maximum value is set. The proposed temperature control loop is implemented by the CU located in the DC/DC converter (see section 2.4). The VI is connected to the CU to monitor and display the evolution of the variables of interest (see Fig. 2(b)).

3.2.3. Electrical subsystem design and implementation

The electrical subsystem integrates all the protections, interconnection, and electrical measures necessary for a safe power supply to the load. For this purpose, the BoP is completed with the inclusion of a non-return diode (7, Fig. 3) and a high-current safety relay (8, Fig. 3). These elements ensure unidirectional current flow towards the load and electrical isolation during controlled shutdown of the stack, respectively.

Finally, the current and voltage sensors (9 and 10 respectively, Fig. 3) are used to measure the operating point of the stack, to carry out the necessary control loops depending on the operating voltage, current or power, and to detect possible problems due to high currents, short circuits or low voltages due to insulation problems between cells. These sensors are integrated in the power stage of the DC/DC converter (see section 2.4). The control of the safety-relay and the measurement of electric parameters are implemented by the CU located in the DC/DC converter (see section 2.4).

3.3. DC/DC power converter

For the proper integration of the AC-MSFCS into the HVDC bus, an isolated push–pull converter topology has been chosen (Fig. 5), which is connected to each stack output (Fig. 2(b)). The choice of this isolated DC/DC converter topology instead of a conventional non-isolated one, is mainly determined by the following reasons. The guarantee of electrical isolation provided by the transformer, as well as the high lift ratios allowable, which would be difficult to achieve with non-isolated topologies, or which would lead these converters to operate in regions with strongly non-linear behaviour and unsuitable efficiency. Electrical isolation between the source and load allows safe operation of elements

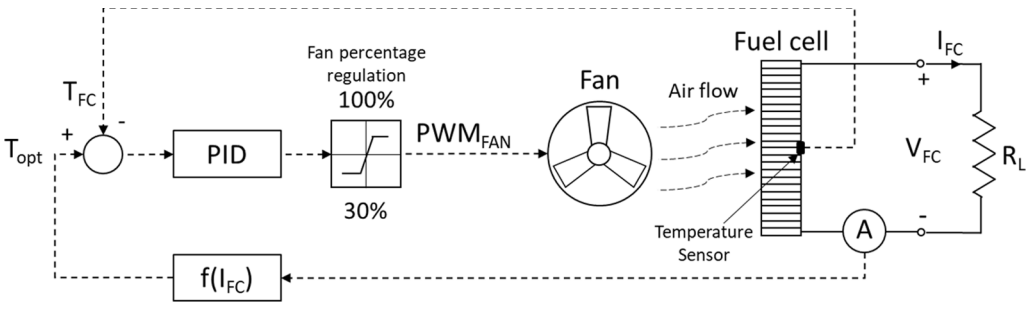

Fig. 4. Stack temperature controller.

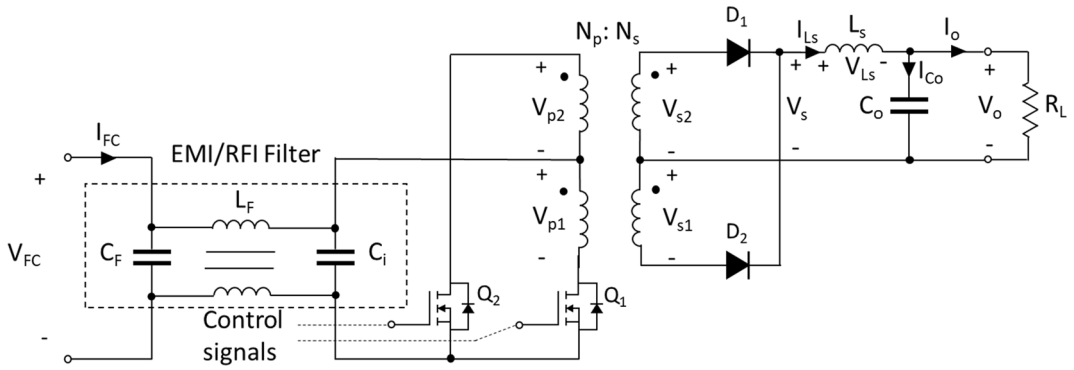

Fig. 5. Scheme of the developed DC/DC converter.

connected to a HVDC bus, even more so when operating with high-cost elements, as in this case FCs. As for the lift ratio of the converter it must be very high (>1:10), as it must be taken into account that ACFCs supply a low voltage output, so it is a challenge to connect them to a HVDC bus. Moreover, compared to other isolated topologies, the use of a push–pull architecture makes it possible to reduce conduction losses with respect to flyback, forward or half-bridge topologies, due to the use of low currents in the primary; as well as with respect to full-bridge topology, which requires a greater number of semiconductors [48].

In this case, due to the lack of commercially available solutions, an ad hoc design of a high performance 3 kW isolated push–pull converter has been made (Fig. 5). Also, an input filtering stage has been included with the aim of reducing the ripple current stack, which is decisive to reduce its operating stress and accumulated degradation [44,49]. Due to the wide availability of commercial filters for industrial power electronics applications, the selected filter is a commercial EMI (Electromagnetic Interference) / RFI (Radio Frequency Interference), whose technical specifications are within the range of this application. Specifically, the Schaffner® FN2410-80-34.

3.3.1. DC/DC power converter model

The electronic switches Q1 and Q2 (MOSFET transistors) in Fig. 5 are activated following a control sequence and never at the same time to avoid short-circuits. Then, calling the total duration of the control signal (following this sequence of activation: (Q1 on + Q2 off) + (Q1 off + Q2 off) + (Q1 off + Q2 on) + (Q1 off + Q2 off)) as T, the duty cycle, δ, of each electronic switch, is the fraction of time where Q1 or Q2 are on. This is, $\delta = t_{on}/T$. So, if for example $\delta = 0.25$, this means that each switch is on for a quarter of the total duration of the control pulse T. Of course, following mentioned activation sequence, the delay between the activation of Q1 and that of Q2 must always be $T/2$. Since both transistors should never be on at the same time, the duty cycle limit is 0.5.

Considering ideal components (it is enough for this analysis), When Q1 is on and Q2 is off (case 1), and Q1 is off and Q2 is on (case 2), V_{FC} and I_{FC} are applied to the lower and upper primary winding respectively, inducing voltage in the secondary windings according to the polarity defined by the dot convention (Fig. 6). Therefore, D_1 will conduct and D_2 will not and vice versa for cases 1 and 2 respectively. The equivalent circuit in the secondary is similar in both cases to that of a buck converter with the switching device in the conduction state, Fig. 6(a). Then, $v_s(t) = v_{FC}(t)(N_s/N_p)$, where N_p and N_s are, respectively, the number of turns of the primary and secondary windings of the transformer.

Assuming a constant output voltage V_o due to the high-capacity capacitor C_o, the voltage in L_s is also a constant and the current in L_s increases linearly. Based on the above and in accordance with the equivalent circuit of Fig. 6(a), the equations modeling the current and voltage behavior of the output filter capacitor and inductor are presented in equations (12) and (13).

$$i_{C_o}(t) = C_o\frac{dv_{C_o}(t)}{dt} = i_{L_s}(t) - i_o(t) \rightarrow \frac{dv_{C_o}(t)}{dt} = \frac{i_{L_s}(t)}{C_o} - \frac{v_{C_o}(t)}{R_L C_o} \quad (12).$$

$$v_{L_s}(t) = L_s\frac{di_{L_s}(t)}{dt} = v_s(t) - v_{C_o}(t) \rightarrow \frac{di_{L_s}(t)}{dt} = \frac{v_s(t) - v_{C_o}(t)}{L_s} \quad (13).$$

On the other hand, when Q1 and Q2 are off (case 3), the current in the two primary windings is zero, so the induced voltage in each secondary winding is zero as well, i. e., $v_s = 0$. However, regardless of the near-instantaneous transitions of the electronic switches, the current in the inductor must maintain continuity, so D_1 and D_2 will conduct. The inductor current is then divided evenly between the two secondary windings of the transformer. The equivalent circuit in the secondary is similar in both cases to that of a buck converter with the switching device in the non-conduction state, Fig. 6(b). Since their voltages are zero (remember it is considering ideal components), $v_{L_s}(t) = v_s(t) - V_o = -V_o$, which produces a linear decrease in current in L_s. Based on the above and in accordance with the equivalent circuit of Fig. 6(b), the equations that model the behavior of the current and voltage of the capacitor and inductor of the output filter, $i_{C_o}(t)$ and $v_{L_s}(t)$ respectively, are presented in equations (14) and (15).

$$i_{C_o}(t) = C_o\frac{dv_{C_o}(t)}{dt} = i_{L_s}(t) - i_o(t) \rightarrow \frac{dv_{C_o}(t)}{dt} = \frac{i_{L_s}(t)}{C_o} - \frac{v_{C_o}(t)}{R_L C_o} \quad (14).$$

$$v_{L_s}(t) = L_s\frac{di_{L_s}(t)}{dt} = -v_{C_o}(t) \rightarrow \frac{di_{L_s}(t)}{dt} = \frac{-v_{C_o}(t)}{L_s} \quad (15).$$

Considering the current and voltage of the capacitor and inductor, respectively, as state variables, and the FC output voltage $v_{FC}(t)$ as input variable, the state-space model for the converter (16), is obtained from (12) to (15). For the instantaneous value of the converter model, the duty cycle takes values of 0.5 and 0 during the time intervals t_{on} and

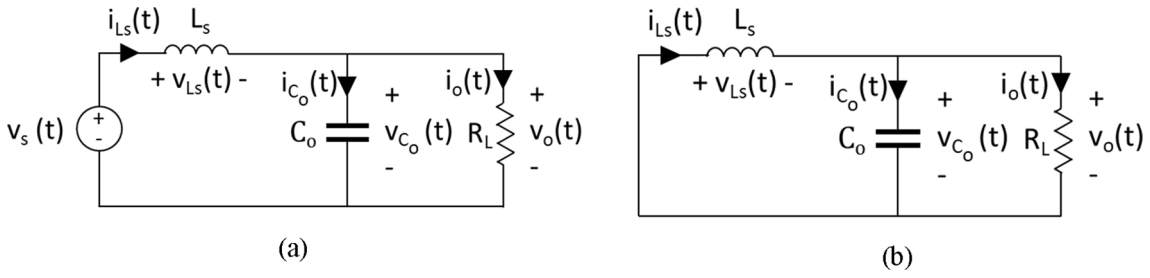

Fig. 6. (a) Equivalent circuit for Q1 or Q2 on, case 1 and case 2; (b) Equivalent circuit for Q1 and Q2 off, case 3.

$T - t_{on}$, coinciding with the practical limit of the duty cycle of each transistor. For the average value of the model, the duty cycle takes values between 0 and 1, coinciding with the duty cycle of the converter.

$$\begin{bmatrix} \dot{i}_{L_S} \\ \dot{v}_{C_o} \end{bmatrix} = \begin{bmatrix} 0 & -\frac{1}{L_s} \\ \frac{1}{C_o} & -\frac{1}{R_L C_o} \end{bmatrix} \begin{bmatrix} i_{L_s} \\ v_{C_o} \end{bmatrix} + \begin{bmatrix} 2\delta \frac{N_s}{L_s N_p} \\ 0 \end{bmatrix} [v_{FC}] (16).$$

To facilitate the design of the different control algorithms required (section 2.3.3), voltage and power control, the model outputs will be defined as the converter output voltage and current, according to expressions (17) and (18), presented in matrix form in (19).

$v_o(t) = v_{C_o}(t)$(17).

$i_o = \frac{v_o(t)}{R_L} = \frac{v_{C_o}(t)}{R_L}$(18).

$$\begin{bmatrix} i_o \\ v_o \end{bmatrix} = \begin{bmatrix} 0 & \frac{1}{R_L} \\ 0 & 1 \end{bmatrix} \begin{bmatrix} i_{L_s} \\ v_{C_o} \end{bmatrix} (19).$$

The output voltage and current can be calculated from the model developed in (19) for the steady state (null state vector), resulting in equations (20) and (21).

$V_o = 2V_{FC}\frac{N_S}{N_P}\delta$.(20)

$I_o = 2V_{FC}\frac{N_S}{R_L N_P}\delta$.(21)

3.3.2. DC/DC power converter design and implementation

First, it is necessary to define the operating parameters of the converter. For that, it must be taking into account that the minimum value of V_{FC} is 40 V and the maximum 80 V (the inevitable deterioration of the stack will cause its voltage to drop from when it was brand new (80 V) to useless (40 V); moreover, although the stack may be new, in some cases it may not be in the best interest to work at full power, for example, to save hydrogen. On the other hand, although the rated voltage on the DC bus is 360 V, as the battery bank is directly connected to the DC bus, when the batteries are fully charged it can reach 420 V. Finally, it is necessary to set the frequency of operation of the converter and its maximum duty cycle. Regarding the first, considering the recommendation of the transformer core manufacturer, frequencies from 10 to 50 kHz were tested. The one chosen as offering the best performance was 20 kHz, which, by the way, is a typical frequency of operation of power converters. As will be seen, the operating frequency completely characterizes the size and quality of the converter components and, ultimately, its performance and losses, so it is very important to choose the most suitable frequency. Finally, as for the duty cycle, as mentioned above, its limit is 0.5, so a conservative maximum value may be 0.45.

- Transformer core sizing

The first step, the sizing of the transformer core, is based on the determination of the minimum dimensions necessary to guarantee the maximum magnetic flux associated with the design active power of the converter (3000 W) at its operating frequency. For this purpose, the empirical equation (22), provided by Unitrode® and Texas Instruments® for the design of power transformers in switching power supplies is used [50]. This equation is based on the core area product (AP), obtained by multiplying, in cm^2, the core magnetic cross-section area A_E by the window area available for the winding A_W. This allows obtaining the product of the minimum areas of the core that guarantee the design power under certain operating frequency restrictions, core material and maximum allowed magnetic flux, with the objective of ensuring that the core always operates within its linear region.

$$AP = A_E A_W = \left(\frac{P_o}{C \bullet \Delta B \bullet f_T}\right)^{\frac{4}{3}}.(22)$$

Where:

P_o: output power (W).

C: 0.014 (forward converter, PPCT); 0.017 (push–pull, full bridge, half bridge).

ΔB: Flux density deviation swing (Tesla, T).

f_T: Transformer operating frequency (Hz).

As explained in the operation of the converter, current always flows through its inductor, which means that the converter operates in continuous conduction mode. In this operation mode, the AC flux component is relatively small, therefore, the limitation in the variation of the flux density is usually limited by saturation, not so much by losses in the core. This implies that the best choice for the magnetic core material is a P-type (Zinc based ferrites). P-type magnetic materials have a higher saturation flux density and higher permeability than K-type materials (Silicon-iron based composites in very high frequency applications) [51].

In this case, considering the selected operating frequency of the converter (20 kHz), a core of NiZn material (N27 ferrite) has been chosen. Based on the core loss curves of this material, and to work in the linear region, a ΔB limit of 500 mT (250 mT positive and negative during core magnetization and demagnetization) has been set. Then, applying (22), the minimum required AP is (23).

$$AP = \left(\frac{3000}{0.017 \bullet 0.5 \bullet 20000}\right)^{\frac{4}{3}} = 45.94 \text{ cm}^4.(23)$$

Based on the obtained AP, the ferrite EPCOS© E100/60/28 core has been selected (its $A_E = 7.35$ cm^2, $A_W = 6.90$ cm^2, so $AP = 50.715$ cm^4).

- Calculation of the number of turns of the primary and secondary winding of the transformer.

The application of Faraday's law to an inductor with N turns of wire allows to obtain the induced voltage (V), which is given by equation (24).

$V = -N\frac{\Delta Đ¤}{\Delta t}$.(24)

Where:

Đ¤: magnetic flux intensity (Wb).

The minus sign that gives the sense of the induced voltage has been omitted as it does not influence the calculations that follow. Now, if $\Delta t = t_{on}$, (7) can be written as (25).

$Vt_{on} = N \bullet \Delta Đ¤ = N \bullet \Delta B \bullet A_E$.(25)

Then, considering that $t_{on} = \delta / f_T$, (24) can be written as (26).

$N = \frac{V \bullet \delta}{\Delta B \bullet A_E \bullet f_T}$.(26)

In this case, $V = V_{FC}$ and $N = N_P$, but what value of V_{FC} should be considered? Well, analyzing (20) it is easy to see that as N_S/N_P will be a constant, the way to have the bigger regulation window is to calculate N_S/N_P with $V_{o,max}$, $V_{FC,min}$ and δ_{max}, this is (27).

$\frac{N_S}{N_P} = \frac{V_{o,max}}{2V_{FC,min} \bullet \delta_{max}} = \frac{420}{2 \bullet 40 \bullet 0.45} = \frac{70}{6}$.(27)

Then, from (27), N_P will be (28).

$N_P = \frac{40 \bullet 0.45}{0.5 \bullet 0.000735 \bullet 20000} = 2.45$.(28)

Therefore, by choosing $N_P = 3$, (10) provides that N_S can be set to 36.

- Output low-pass filter.$L_s - C_o$

Referring to Fig. 5, when Q1 or Q2 is on, the relationship between current and voltage at L_s is given by (13), which can be written as (29).

$$\frac{\Delta I_{L_S}}{\Delta t} = \frac{V_{L_S}}{L_s} = \frac{(V_s - V_o)}{L_s} = \frac{\left(\frac{N_S}{N_P}V_{FC} - V_o\right)}{L_s}.(29)$$

Again, if $\Delta t = t_{on} = \delta / f_T$, (29) can be written as (30).

$$L_s = \frac{\left(\frac{N_S}{N_P}V_{FC} - V_o\right)\delta}{\Delta I_{L_S} \bullet f_T}.(30)$$

As ΔI_{L_S} is the swing of the current in the inductor L_s during t_{on}, in practice, it is the ripple. But looking at (30), if a small ripple is desired, the result will be a large inductor, however, as is well known, the most non-linear element in a DC/DC converter is by far the inductor (as a rule of thumb / empirical, multiplying by 2 its inductance means multiplying

by 1.5 its internal resistance), so this should be as small as possible. With all this in mind, it is best to assume a relatively high ripple which can then be damped with a high-capacity output capacitor (the actual behavior of a quality capacitor is much closer to the ideal than that of an inductor). So, assuming $\Delta I_{L_s} = 30\%$ and using extreme values as in (27), the L_s value is obtained by (31).

$$L_s = \frac{(12 \bullet 40 - 420)0.45}{0.3 \bullet \frac{3000}{420} \bullet 20000} = 0.00063\text{H}. \quad (31)$$

Therefore, a 630 μH inductor is chosen.

Regarding the output capacitor C_o, according to Fig. 5, its current and voltage are given by (12), which allows to write (32).

$$\frac{\Delta V_{Co}}{\Delta t} = \frac{I_{Co}}{C_o}. \quad (32)$$

Again, if $\Delta t = t_{on} = \delta / f_T$, C_o is given by (33).

$$C_o = \frac{I_{Co} \bullet \delta}{\Delta V_{Co} \bullet f_T}. \quad (33)$$

where I_{C_o} will be the one corresponding to the ripple in L_s. So, assuming a voltage variation at the output of only 0.5% (this will keep V_o constant, as desirable), and using, again, extreme values, the C_o value is obtained by (34).

$$C_o = \frac{0.3 \bullet \frac{3000}{420} \bullet 0.45}{0.005 \bullet 420 \bullet 20000} = 2.30 \times 10^{-5} F \quad (34).$$

Therefore, a 25 μF capacitor is chosen.

3.3.3. Design of the fuel cell control loops

In the usual configuration, each FC can be either on or off (meaning zero or rated power), however, since current and voltage measurements are available for each FC and converter assembly (see Figs. 3 and 5), and therefore power (integrating, also energy), it would be possible to regulate both output voltage and power of each of the FC lines.

As (20) and (21) indicates, the control of the DC/DC converter output is done by δ. So, the way to regulate it is by pulse width modulation (PWM). This implies that the DC/DC controller must be a PWM controller. In this case, the pulse width is generated by two PID controllers depending on the type of control to be implemented in each FC line, namely output voltage control or output power control. Depending on the application, the EMS will automatically select the control mode depending on the desired function to be performed by the AC-MSFCS (as a whole or in part of its FC lines).

In particular, the voltage control allows the DC bus voltage to be adjusted when the battery bank has a reduced state of charge, allowing the AC-MSFCS to be used as a voltage-controlled battery charger. On the other hand, the power control will allow to set the power injected to the DC bus if the reference power is lower than the nominal power of each stack, typical of conservative strategies aimed at reducing hydrogen consumption, or to test a specific stack, increasing the versatility of the system.

In the first instance, the output voltage control loop scheme for each FC is shown in Fig. 7, and it is implemented in the CU (section 2.4). The variable to control is the output voltage V_o of each converter. As for the control law, it is very simple, the controller receives the measurement of V_o and compares it with the reference voltage V_{ref}. The error signal will be the controller input to generate the δ that equals V_o to V_{ref}. The voltage reference is usually the rated DC bus voltage and is set by the EMS, however, in case of low state of charge of the battery bank, hydrogen surplus and lack of renewable resource, the EMS raises the V_{ref}, so that the FC and converter assembly can be used as a battery bank charger.

Finally, the schematic of the output power control loop for each FC line is shown in Fig. 8 and, again, it is implemented in the CU (section 2.4). To ensure the correct power supply to the DC bus, and considering the losses associated with the power stage, the controlled variable is represented by the output power P_o of each FC line. The proposed tracking problem poses a one-input, multiple-output control problem (input: duty cycle, outputs: output voltage and output current). To employ the PID control technique, the control loop can be simplified to a current control loop, considering that the converter output voltage V_o is constant between two sampling periods (this is achieved by the correct design of the converter output capacitance C_o and the direct connection of the battery bank to the DC bus). Based on the above, for the implementation of the control law, the controller receives the V_o and I_o measurements and compares the latter with the reference current I_{ref}, calculated from the quotient between P_{ref} and V_o. The error signal will be the controller input to generate the δ that equals I_o to I_{ref} and, consequently, P_o to P_{ref}. The implementation of the tracking problem with respect to the setpoint power of the AC-MSFCS, allows to increase the performance of the system when its setpoint is obtained from the implementation of the EMS optimization strategies [52].

3.4. Control unit design and implementation

In order to achieve a compact AC-MSFCS, minimizing the number of elements, a single CU has been developed for each FC line, which is responsible for managing its BoP, the DC/DC converter and bidirectional communications with the VI and EMS (Fig. 2(b)). The CU allows to use every stack connected or not connected to the DC/DC converter, so the AC-MSFCS also functions as a work bench for teaching and research purposes.

To this end, the CU performs the acquisition of the FC control variables, the generation of the solenoid valves and safety relay control signals, the control of the cooling/stoichiometry system and the DC/DC converter. In addition, it carries out the management of events and startup and shutdown procedures during normal operation or system errors. For this purpose, specific high-performance acquisition and

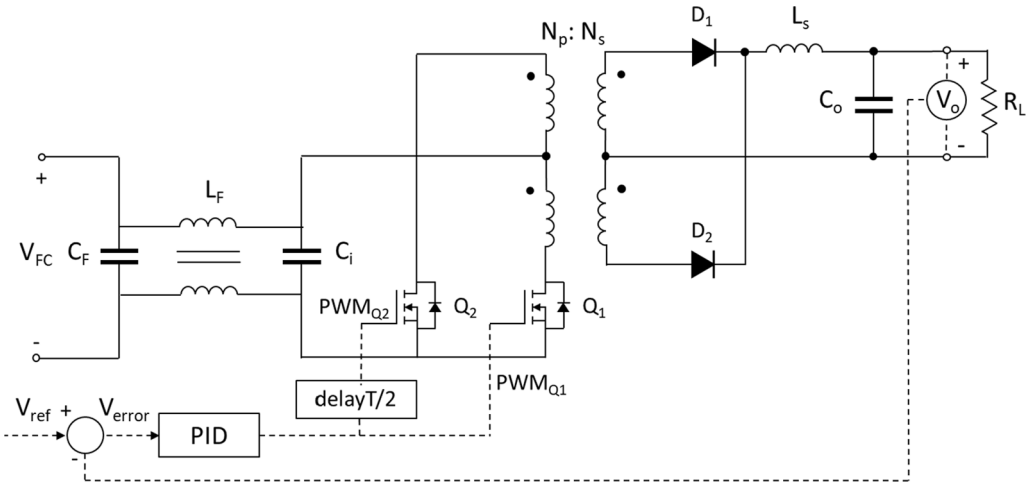

Fig. 7. Fuel cell output voltage control loop.

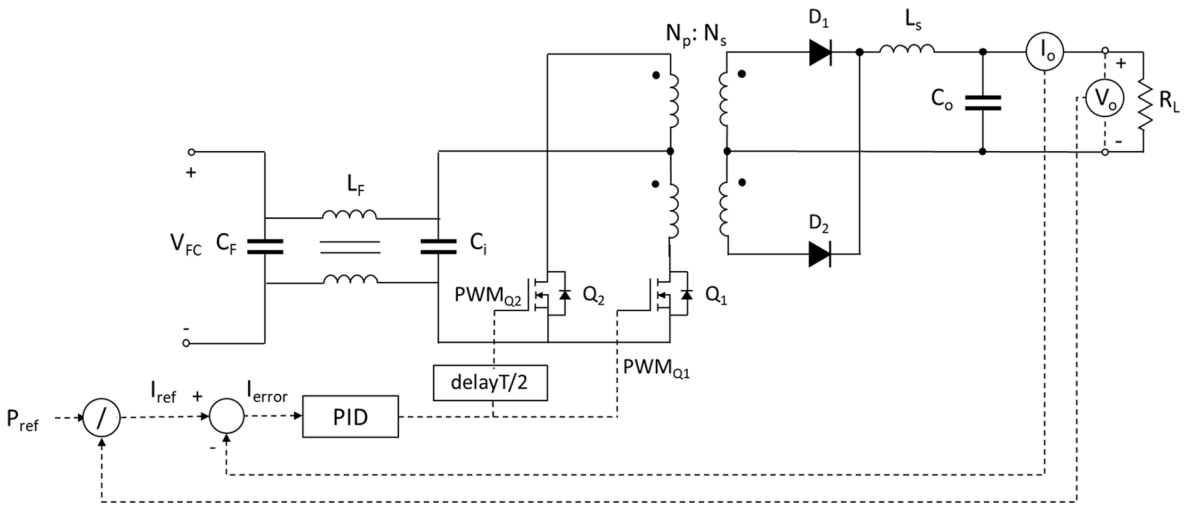

Fig. 8. Fuel cell output power control loop.

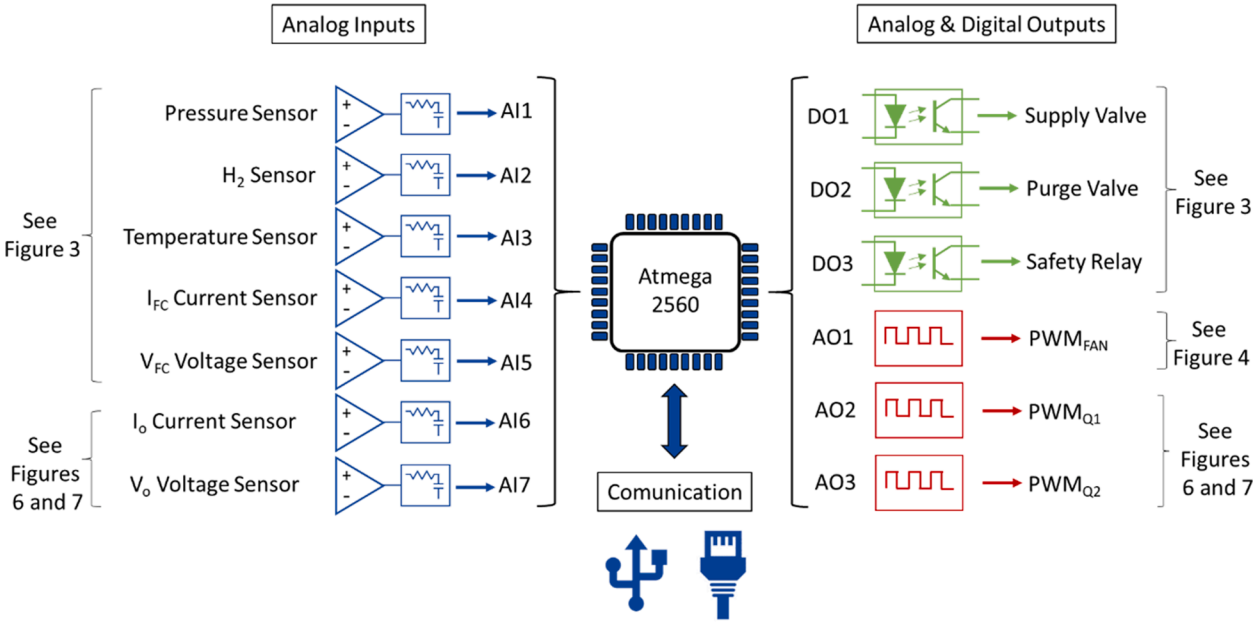

Fig. 9. CU architecture.

control electronics has been developed. It is based on the ATmega2560 microcontroller programmed in the Arduino IDE environment, please see Fig. 9.

Considering the acquisition electronics, a different signal conditioning circuit has been designed for the measurement of each analogue variables, depending on the type of signal and its parameters (voltage, current or resistance). These circuits are based on the use of operational amplifiers in differential configuration, first-order analogue filters and the use of the microcontroller's ADC converter (analog inputs (AI), Fig. 9).

For the thermal control of each stack and the generation of each DC/DC converter control signals, the CU generates three PWM signals (analog outputs (AO), Fig. 10). The δ of these signals determines the stack cooling air flow rate, according to the stack temperature controller (Fig. 4), and the output voltage/power of each FC line, according to the controllers presented in Figs. 7 and 8 respectively.

Finally, to control the discrete elements (electrovalves and safety relay), driver circuits based on low power optocouplers and mosfets have been implemented with the aim of ensuring electrical isolation (digital outputs (DO), Fig. 9).

Fig. 10 presents the practical implementation of the developed design in this section: DC/DC converter and CU. Both are housed in the same plate although, obviously, in different electronic boards. Table 3 shows the main characteristics of the devices that make up the DC/DC power converter and CU.

3.5. VI design and implementation

To control, manage and monitor the entire AC-MSFCS, and as a part of it (Fig. 2(b)), a powerful VI has been developed in the LabVIEW® interface. The VI includes all the necessary functions to ensure bidirectional communication with the CU (via USB or Ethernet connection,

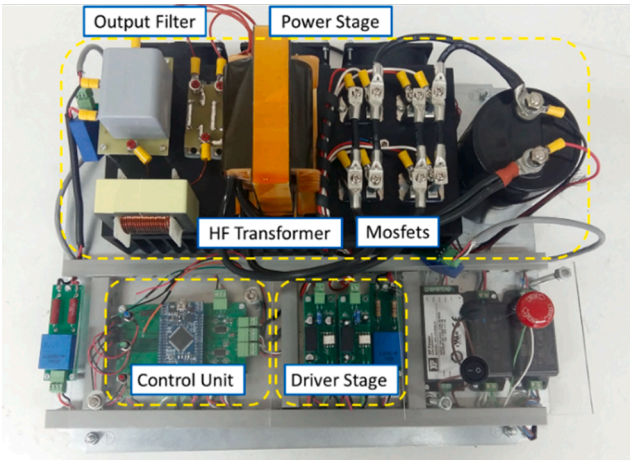

Fig. 10. Physical implementation of the developed DC/DC converter, its principal parts and CU.

Table 3
Main parameters of the power converter and CU components.

Element	Model	Characteristics
Microcontroller	ATmega2560, Microchip®	Supply voltage: 5 VDC Architecture: 8-bit AVR RISC CPU speed: 16 MHz
Current sensor	LA 55-P-SP1, LEM®	Supply voltage: ±12-15 VDC Measurement range: ±100 A Output current: ±25 mA
Voltage sensor	LV25-P, LEM®	Supply voltage: ±12-15 VDC Measurement range: ±14 mA Output current: ±25 mA
EMC/RFI Input filter	FN2410-80–34, Schaffner®	Operating frequency: DC-400 Hz Rated voltage: 300 VDC Rated current: 80 ADC
MOSFET Gate driver optocouplers	FOD3182, FAIRCHILD®	Supply voltage: ±20 VDC Voltage isolation: 4000 V Output current: 3 A
MOSFET	IXFN132N50P3, IXYS®	Maximum voltage: 500 V Maximum current: 112 A Static drain-source on resistance: 39 mΩ
Transformer	Custom, Saber S.L. ®	Operating frequency: 20 kHz Ferrite material: N27 Rated power: 3000 VA Winding turns ratio: 1:12
Diode	VS-20ETF12PbF, Vishay®	Maximum voltage: 1200 V Maximum current: 20 A Forward voltage: 1.31 V
Output capacitor	MKP1848625454P4, Vishay®	Rated capacity: 25 μF Maximum voltage: 800 V
Inductor	Custom	Inductance: 0.63 mH Operating frequency: 20 kHz Ferrite material: N27

Fig. 9), allowing to govern the start, stop and reset of each FC and its DC/DC converter, as well as the control loop to be implemented, voltage or power. Similarly, it is possible to manually define the power/voltage setpoint of each DC/DC converter (the EMS does it automatically), (1, Fig. 11(a)). The main VI control panel is shown in Fig. 11(a). In it, the status of each FC and its corresponding DC/DC converter can be monitoring, (2, Fig. 11(a)).

For each individual FC, an intuitive control panel has been designed (Fig. 11(b)). This panel allows the state of the various elements that make up the BoP to be graphically displayed (solenoid valves, safety relay and percentage of fan speed regulation), as well as the main stack parameters: hydrogen supply pressure, temperature, voltage, current and power, as well as the hydrogen concentration.

A specific panel has also been developed for the graphical representation of the operating point and temperature of each stack, with respect to the manufacture polarization curve and the temperature limits according to the operating current: minimum, maximum, optimum (reference) and robust temperature (1, Fig. 12(a)). This interface allows to check the deviation of the current operating point of the stack from the theoretical one, quantifying the accumulated degradation of each stack. Likewise, in case a detailed study of the individual degradation of the cells of each stack is required, the SCADA integrates all the functionalities for the correct integration of the cell voltage monitoring system patented and developed by the research group [19,40], (Figs. 2, 12(a)). This information can be used by the EMS for the implementation of a power generation distribution according to the degradation of each stack, as well as the performance of preventive maintenance tasks by the end user.

As for each FC line, there is a specific panel for the control and management of each DC/DC converter (Fig. 12(b)). On this panel, the main electrical parameters of the DC/DC converter, i. e., input and output voltages and currents, as well as its operating temperature are displayed, (1, Fig. 12(b)). In the same way, there is an alarm panel and status display, from which the status of the converter can always be known and, in the event of an error, the cause that has produced it, (2, Fig. 12(b)).

The main errors are given by the correct operation of the DC/DC converter, as well as by the maximum and minimum operating limits of the FC and the DC bus. Thus, the event caused by the emergency stop, the error due to low and high input voltage from the FC and to the DC bus, as well as the FC overcurrent and the DC/DC converter over temperature are displayed (3, Fig. 12(b)).

Finally, a specific alarm panel has been designed (Fig. 13), which allows identifying the error condition or event produced in the MSFCS. The implemented alarms collect the events of temperature, pressure, current, voltage and hydrogen leakage. Table 4 shows the activation values for the different AC-MSFCS alarms. These values coincide with the lower and upper values that will delimit the safe and correct operation for the AC-MSFCS.

Finally, Fig. 14 shows the developed AC-MSFCS. It has been housed in an easily accessible cabinet to be used as a demonstrator for teaching and research as well as for technology transfer to companies.

4. Experimental results and discussions

The objective of this section is the experimental validation of the proposed design for the management, control, and integration of AC-MSFCS in high-voltage DC microgrids. Because the proposed system performs individual control and management of each AC-MSFCS stack, it can be easily scaled up by using similar units, and therefore only one fuel cell-BoP-power converter assembly has been tested. The results obtained from these tests can be easily extrapolated to the AC-MSFCS.

To validate the behavior of the developed AC-MSFCS, the EMS power setpoint input was simulated as an ascending and descending staircase power demand profile, whose maximum value corresponds to the maximum power value currently available in the stack, due to its inevitable accumulated degradation, Fig. 15. This profile is suitable for testing the more complex control loops (temperature and output power of the FC as well as the power supplied to the DC bus), the thermal behavior of the FC, the validation of the electrical behavior of the converter and the indirect testing of the output voltage control loop for charging the battery bank. To this end, in order to specifically analyze the behavior of the MSFCS without disturbances from other elements, all except the AC-MSFCS and the battery bank were disconnected in the

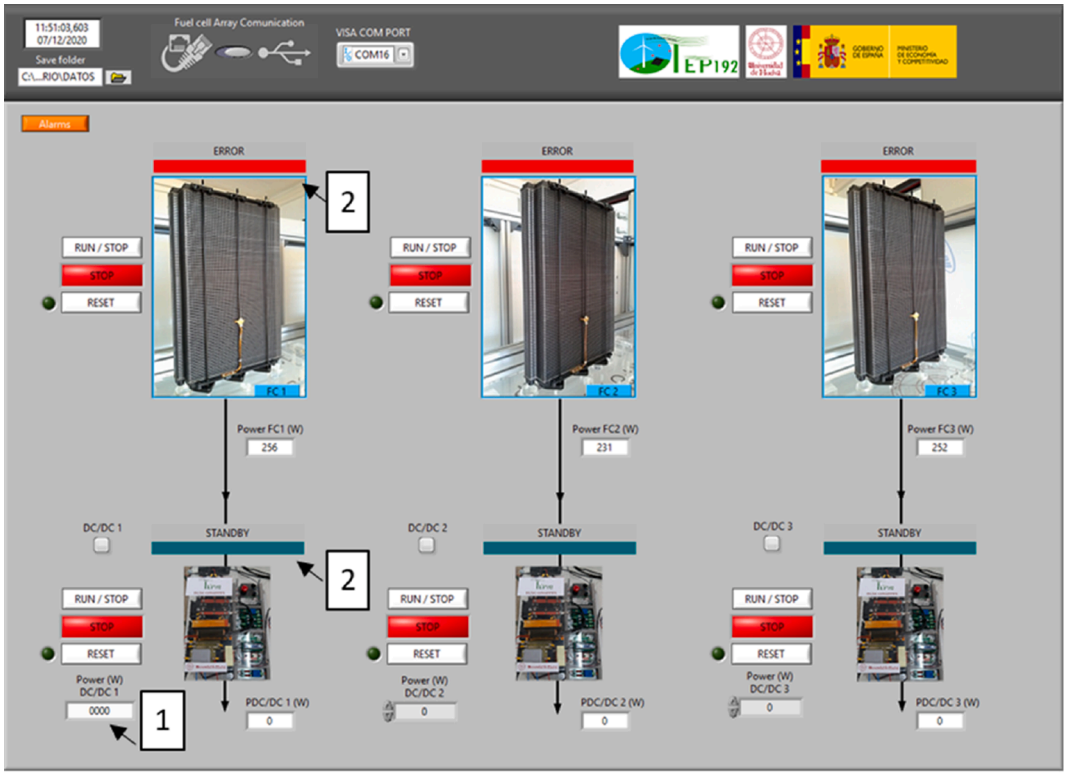

(a)

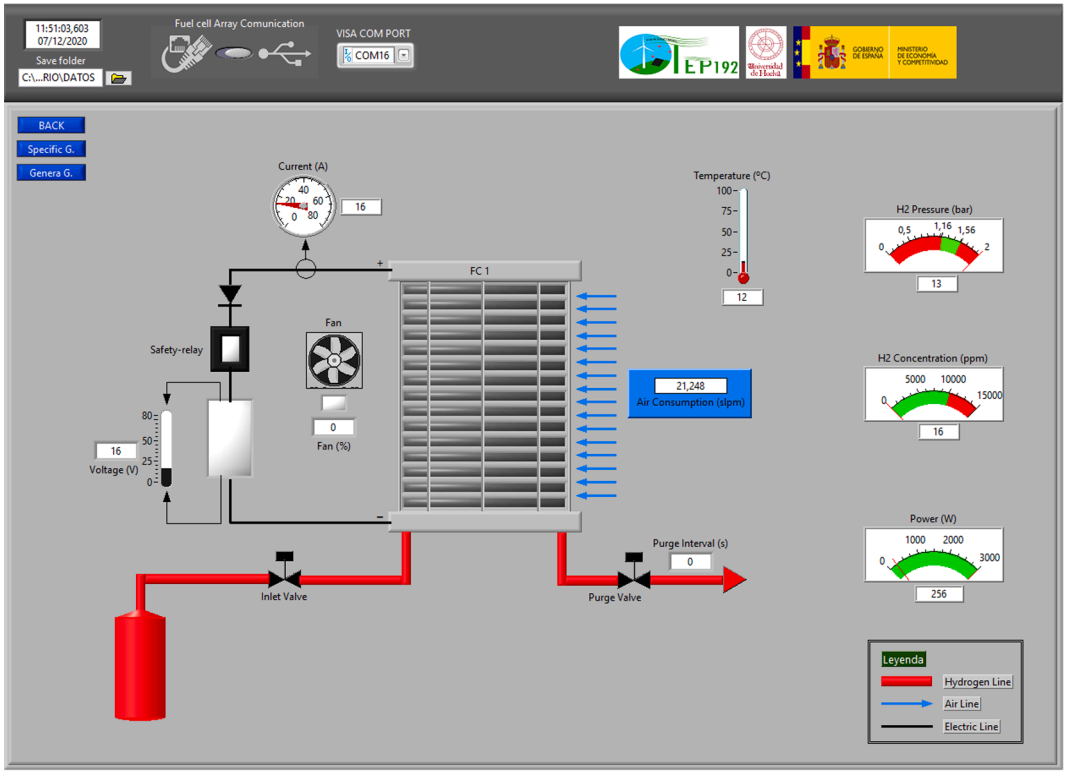

(b)

Fig. 11. (a) AC-MSFCS main control panel; (b) FC parameter monitoring panel.

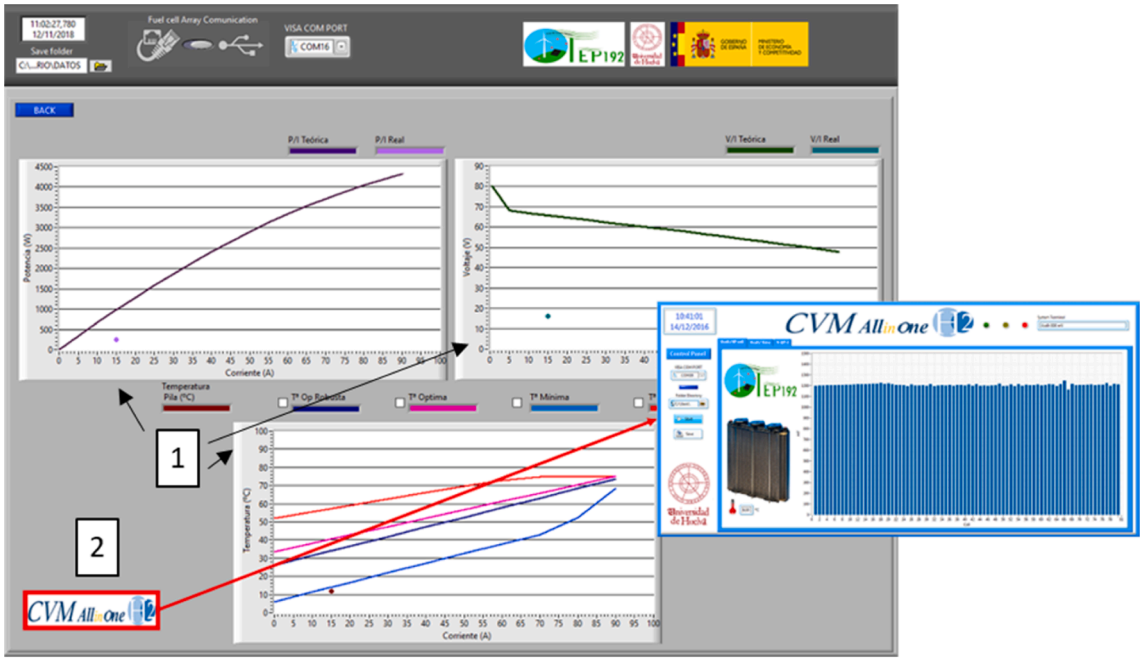

(a)

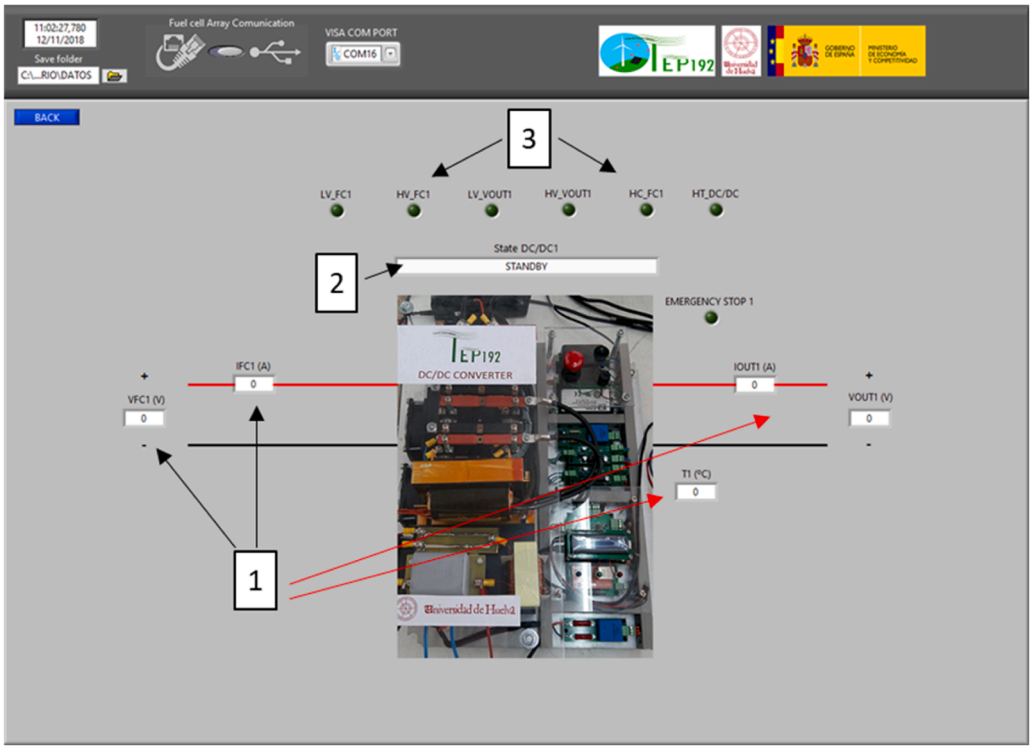

(b)

Fig. 12. (a) Graphical display available for each stack; (b) DC/DC converter control panel.

microgrid (Fig. 1). Thus, the experimental test setup was carried out using a stack along with its BoP connected to the high voltage DC bus via its power converter and CU assembly (Fig. 10). The battery bank was also connected to the bus.

For the acquisition and monitoring of the electrical variables, current and voltage sensors integrated in the power converter and CU assembly (Table 3) were used, as well as a Teledyne LeCroy® WaveSurfer 454 oscilloscope with differential current and voltage probes. On the other hand, for the measurement of cell voltages and the quantification of their cumulative degradation, the CLSMS designed by the authors and presented in [19] was used. For this purpose, each CLSMS probe was connected to each cell in the stack (80 in total). Similarly, the temperature sensor integrated in the BoP (Fig. 3) and a thermal camera model Testo 875®, respectively, were used to monitor the temperature variables of the stack and the developed converter. Finally, the hydrogen supply for the tests was provided by a pressurized hydrogen supply line at 200 bar and two pressure regulation stages in series at 10 and 1.5 bar, respectively.

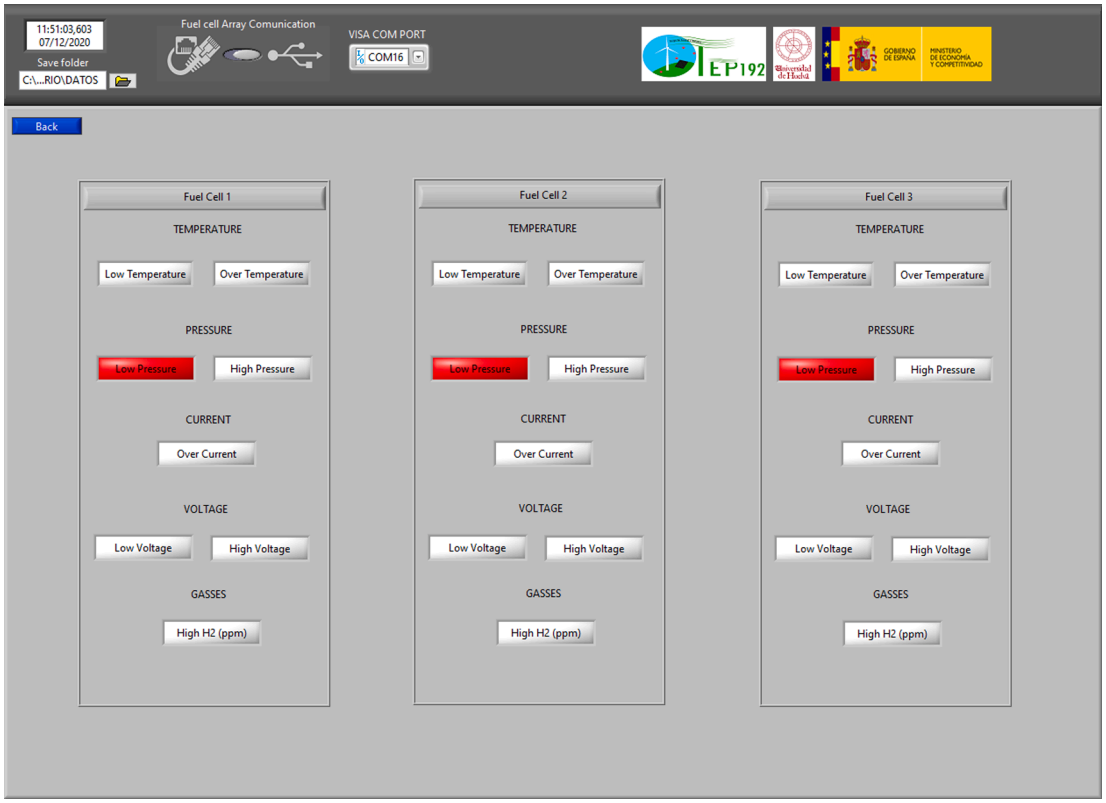

Fig. 13. MSFCS alarm panel.

Table 4
Activation values for the different AC-MSFCS alarms.

Alarm	Error condition
Low voltage in fuel cell (LV_{FC})	Fuel cell voltage < 30 V
High voltage in fuel cell (HV_{FC})	Fuel cell voltage > 85 V
Low voltage in DC Bus (LV_{VOUT})	DC Bus voltage < 330 V
High voltage in DC Bus (HV_{VOUT})	DC Bus voltage > 435 V
Over current in fuel cell (HC_{FC})	Fuel cell current > 70 A
Over temperature in DC/DC converter ($HT_{DC/DC}$)	DC/DC temperature > 80 °C
Low temperature of fuel cell	Fuel cell temperature < $0.539 \bullet I_{FC} + 5$ (°C)
Over temperature of fuel cell	Fuel cell temperature > $0.385 \bullet I_{FC} + 50$ (°C)
Low pressure in hydrogen supply line	H2 Pressure < 1.16 bar
High pressure in hydrogen supply line	H2 Pressure > 1.69 bar
Hydrogen leak (gasses)	H2 concentration > 10000 ppm

Analyzing the results obtained by connecting the AC-MSFCS to the HVDC bus, variables shown in Figs. 15–18 demonstrate the correct operation of the VI (Figs. 11–13), which oversees data acquisition, variable monitoring, and shutdown/startup of the entire AC-MSFCS and, also, of the CU (Fig. 10) which, connected to the VI (also to the EMS), manages the stacks, BoPs and DC/DC converters (Fig. 2(a)).

Thus, Fig. 15 shows the power reference (P_{Ref}) imposed on the controller (see Fig. 8), and the measured variables, namely the FC output voltage (V_{FC}), FC output current (I_{FC}) and FC output power (P_{FC}) for the staircase-type power consumption profile. From the fuel cell variables profiles, the correct behavior of the CU, the BoP management and the power control loop can be indirectly validated.

Specifically, it is verified how the control loop allows to set the desired power (P_{Ref}) at the converter output regardless of the existence of certain non-idealities or disturbances.

The designed control loop allows to cope with intrinsic non-idealities of the system, particularly, the one associated with the efficiency of the converter. This is reflected in the mismatch between the power setpoint and the operating power of the stack (P_{FC}) for the different values of the demand profile. It should not be forgotten that between the fuel cell output and the DC bus is the power converter (see Fig. 2(b)), which has an efficiency <100%. Considering the fuel cell operation point, if a detailed analysis is performed between P_{Ref} y P_{FC} in Fig. 15, it is easy to show, as expected, that the average converter efficiency is around 90%, but this value is not constant, in fact, it has a marked non-linear behavior, depending on the operating point of the fuel cell, as can be seen in Fig. 21. Of course, the closer P_{FC} is to the rated power of the converter, the more efficient the converter will be. Then, for the maximum FC power, the efficiency of the converter is clearly above 90%, however, for the minimum FC power, the efficiency drops clearly below 90%, which obviously coincides with what is expected from Fig. 21.

Similarly, a clear example of how well the controller copes with disturbances is shown in the system response during purge times. As it can be seen, V_{FC} suffers sudden drops spaced over time, that coincide with the purge intervals (remember, every 3000 A.s). Then, as the controller has a setpoint to maintain (P_{Ref}), I_{FC} suddenly increases to follow the reference power.

Now, Fig. 16 shows the DC bus voltage and current. It can be seen from Fig. 16 that the AC-MSFCS, through the DC/DC converter, supplies the load demand and charges the battery bank. In fact, since the SOC of the battery bank is considerably below its maximum, with a voltage correspondence close to 420 V, the increase in the power delivered by the AC-MSFCS raises the DC bus voltage.

An interesting effect, direct cause of the design proposal, is how the DC/DC converter filters (at its input and output, see Fig. 5) virtually eliminate current peaks coming from the FC output (see I_{FC} in Fig. 15). This explains the virtual absence of peaks in $I_{DC.Bus}$ and the smooth profile of $V_{DC.Bus}$.

Considering the degradation of the AC-MSFCS stacks, FC current and voltage monitoring makes it possible to quantify the degradation of the

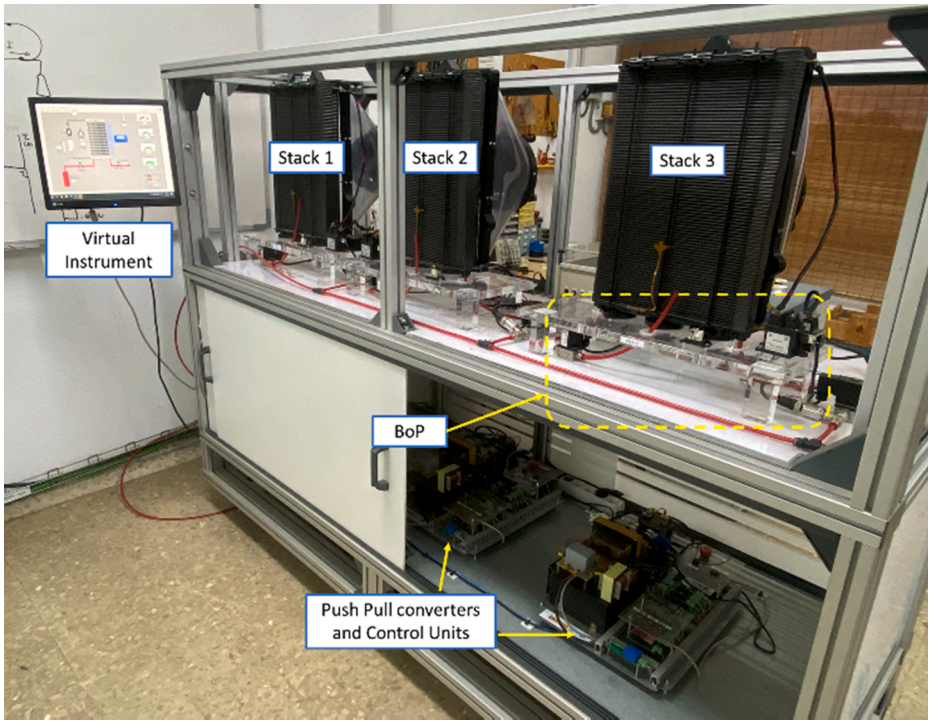

Fig. 14. Physical implementation of the developed AC-MSFCS.

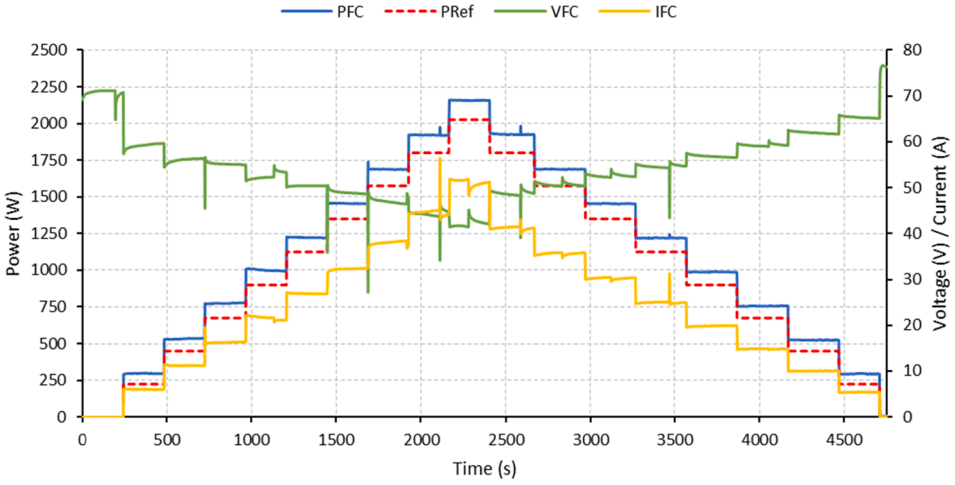

Fig. 15. FC voltage (V_{FC}), current (I_{FC}) and power (P_{FC}) in response to a step-type reference power profile (P_{Ref}) at the FC line.

stack voltage and power for the current conditions, with respect to the theoretical value at the beginning of its lifespan (BoL). Fig. 17 shows the I-V and I-P polarization curves for the initial theoretical case at BoL (V_{Teo} and P_{Teo}), for the upward operation or load increase phase (V_{Up} and P_{Up}) and the downward operation or load decrease phase (V_{Down} and P_{Down}). A discrepancy can be seen between the curves for upward and downward operation, due to the well-known hysteresis phenomenon. This phenomenon is determined by the temperature and moisture level of the membrane. The increase in current after the upward operation causes an increase in water production and, therefore, increases the moisture level in the membrane, which favors proton exchange, thus reducing its resistivity and, with it, the ohmic losses, according to equation (4).

Specifically, according to Fig. 17, a strong voltage degradation is observed in the open-circuit condition with respect to the BoL. A difference of 10 V and 4 V is quantified for the case of the upward and downward operating curve respectively. This discrepancy causes the vertical downward shift of the polarization curve, which will determine the voltage degradation of the stack for different operating current values. In addition, a slight increase in the slope of the voltage curve is observed for the ohmic region of operation ($i_{FC} > 10$ A). This indicates a slight increase in the internal resistance of the membrane and/or electrodes with respect to the BoL. Finally, the measured voltage degradation translates into a power degradation, which for the stack under study, results in a maximum extractable power of approximately 2200 W, coinciding with the values plotted in Fig. 15.

Fig. 18 shows the individual voltages of each of the 80 cells in the stack for a current of 45 A and a stack temperature of approximately 48 °C. Monitoring at high currents has been chosen to allow easier detection of voltage discrepancies between cells. From the results, most of the cells in the stack (1–53 and 74–80) operate at a similar voltage, close to 600 mV, which would mean, if all 80 cells were the same, a stack voltage of approximately 48 V. This is approximately a difference of 11

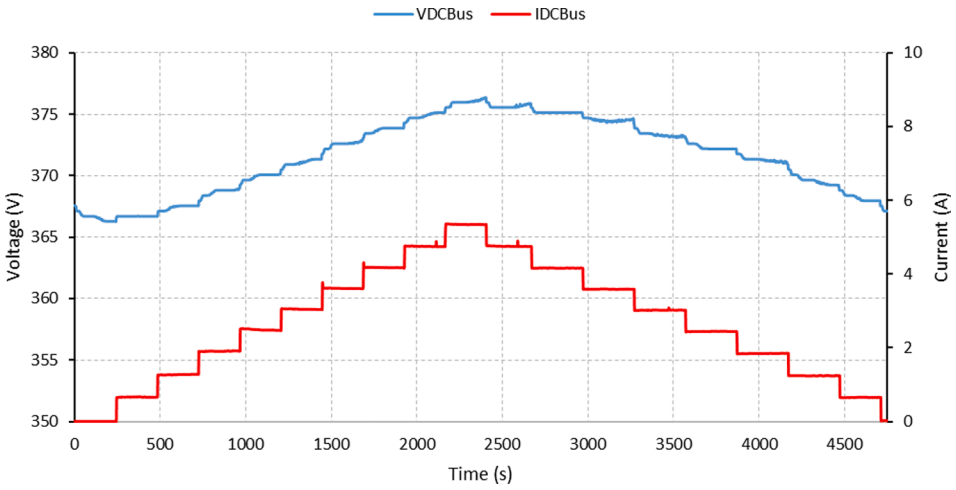

Fig. 16. DC bus voltage ($V_{DC,Bus}$) and current ($I_{DC,Bus}$), in response to a step-type reference power profile at the FC line.

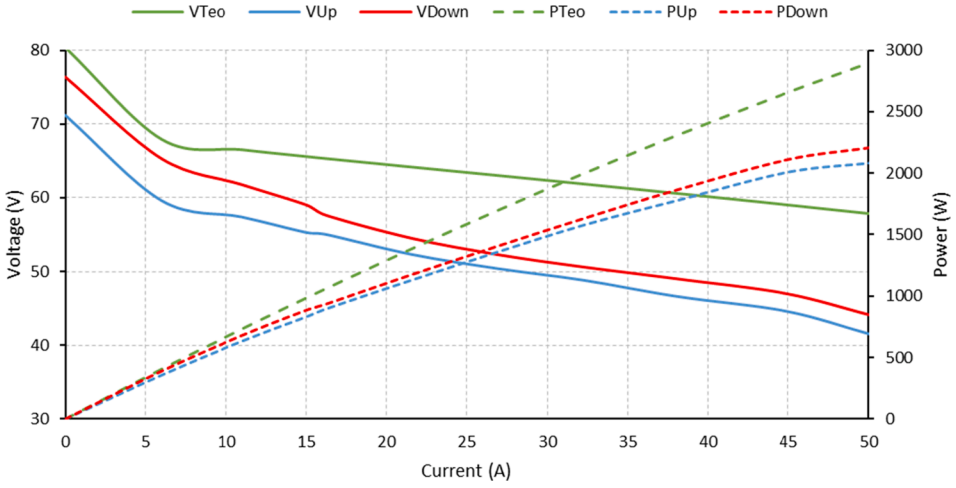

Fig. 17. I-V and I-P polarization curves for the theoretical case (V_{Teo} and P_{Teo}), and experimental curves for the upward (V_{Up} and P_{Up}) and downward (V_{Down} and P_{Down}) load profiles.

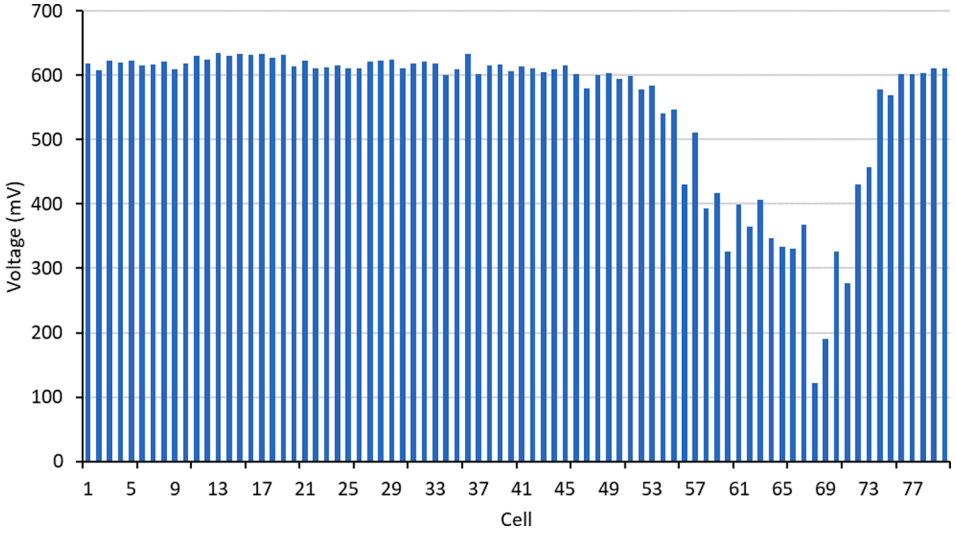

Fig. 18. Individual cell voltage at 45 A.

V with respect to the theoretical case (approximately 140 mV/cell more), which would mean expected and homogeneous degradation. However, as shown in Fig. 17, between cells 54–73, both inclusive, there is a voltage valley zone, reaching a minimum value of approximately 125 mV for cell 68. This phenomenon may be due to different causes, the main ones being the excessive degradation of this cell (note also the effect it has on adjacent cells) and/or the presence of hydrogen leakage due to degradation of the cell sealant. However, the second cause is ruled out, since the BoP hydrogen concentration sensor (4 in Fig. 3) has not detected any leakage. Another proof of this diagnosis is that the presence of hydrogen leaks around cell 68 would cause the voltage drop of all the upper cells due to lack of fuel, which is not seen.

The above information is extremely important, and the AC-MSFCS provides it to the microgrid EMS, which therefore knows the degree of degradation of the stack and the cells that are most deteriorated (at least 68 and 69). This allows it to better manage the power in each line of stacks and, in addition, to warn that corrective maintenance is required to replace the deteriorated cells.

It is very important that the malfunction detected is resolved as soon as possible, since a cell in poor condition will inevitably deteriorate the adjacent cells, causing the effect to multiply until the entire stack is deteriorated.

Regarding the validation of the oxidant/refrigeration controller, Fig. 19 shows the thermal behaviour of the stack, defined by the measured stack temperature (T_{FC}), as well as those calculated by (1), (2) and (3), optimum (T_{Opt}), maximum (T_{Max}) and minimum (T_{Min}) respectively, which are values recommended by the manufacturer.

As can be seen, the temperature of the stack conforms to the optimum (which means that the designed controller, Fig. 19, is working properly), except at low power values. As it has been stated in section 2.2.2, to guarantee the stoichiometry of the reaction, regardless of the temperature of the stack, a minimum air flow rate is set at 30% of the maximum value. This minimum flow rate does not allow the stack to reach its optimum temperature. Obviously, this effect is more pronounced in the upward profile, since in the downward profile the stack is already hot. But this should not be seen as a disadvantage because (1), as the Fig. 19 shows, the stack operates always within the maximum and minimum limits pre-established by the manufacturer and (2), if it is true that working at the wrong temperature contributes to shortening the lifespan of the stack, it is even more true that a FC is designed to work normally at its rated power. Then, as Figs. 15 and 17 show, although the tested stack, due to its deterioration from use, is >1 kW away from its factory rated power, the designed temperature controller works properly around the maximum power it can deliver, around 2200 W.

Another interesting effect shown in Fig. 19 are sudden current peaks. The explanation is obvious, T_{Opt}, $T_{Max}$and T_{Min} are not measured, they are the result of the application of equations (9)-(11) by the VI, so they are affected by the measured current I_{FC} (see Fig. 15).

Next, Figs. 20 and 21 will present the results of the performance validation of the developed power converter in terms of thermal, electrical and efficiency behavior.

Fig. 20 provides very interesting practical information. Thus, Fig. 20 (a) shows a thermography of the developed DC/DC converter at the maximum power achieved in the test (about 2200 W, see Fig. 15). As it can be seen, the temperature in the semiconductors, the transformer and the output filter are around 40 °C, well below the maximum allowed temperature, which is over 100 °C. This means corrects sizing of the DC/DC converter components and, of course, correct sizing of its heat sinks. However, there is an exception in the left corner of Fig. 20(a), where there is a component at about 50 °C, is one of the Hall effect current meters, specifically the one that measures more current (I_{FC}).

Then, Fig. 20(b) shows the current and voltage waveforms at the converter input (FC output) and at the secondary side of the transformer, respectively, for the maximum power. Fig. 20(b) has been obtained using an oscilloscope and represents the duty cycle of the DC/DC converter for the maximum power on the single FC. This figure allows discussing very interesting practical behaviour. First, the very small ripple of the input current to the converter is striking (ocher-colored signal). Considering that the current is scaled with 10 A/div, I_{FC} value is a little >50 A, however, its ripple is only about 1.5 A, so, the ripple percentage is <3%, practically negligible.

The voltage waveform in the secondary winding of the DC/DC converter transformer is shown below in fuchsia-colored, Fig. 20(b). Note the number of oscillations and noise due to transistor switching (as soon as the MOSFET is turned on, its gate capacitance - of high value in power MOSFETs as in this case - behaves as a short circuit to ground; from this point on, as it is charged, the oscillations decrease until they practically disappear), which can hinder measurements, and which are eliminated at the converter output. Then, since the oscilloscope time base is at 10.0 µs/div, 5 div implies a period of 50 µs and, consequently, an operation frequency of the converter of 20 kHz, just as designed. Similarly, at the captured operating point, t_{on} is approximately 20.5 µs, so δ is approximately 20.5/50 = 0.41. With this duty cycle and applying (21), it is easy to check the values of V_{FC} around 40 V (Fig. 15) and $V_{DC,Bus}$ around 375 V (Fig. 16).

Finally, analysing the electrical efficiency of the power converter, Fig. 21 shows the efficiency curves when the converter is working at different input voltages. The input voltages reflect the voltage variation at the FC output.

Note that, in general, above 20% of its rated power (below the duty

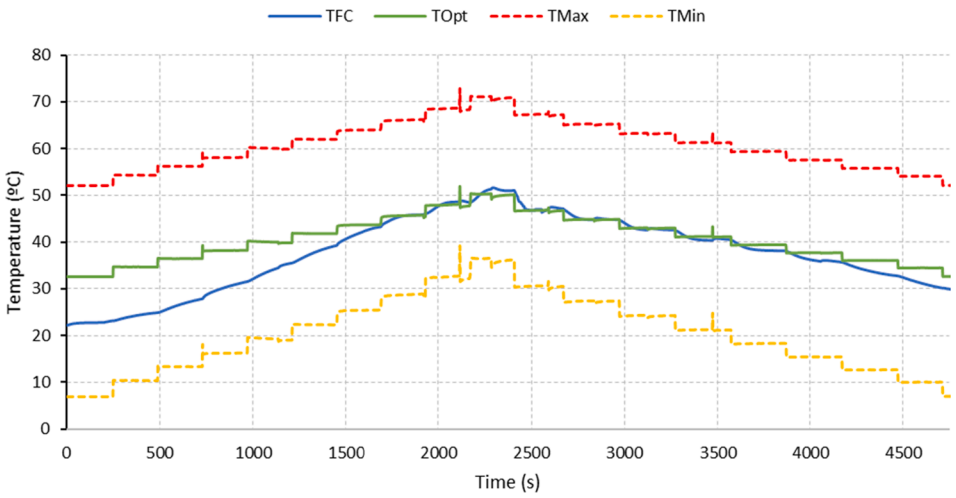

Fig. 19. Measured stack temperature (T_{FC}) and calculated: optimum (T_{Opt}), maximum (T_{Max}) and minimum (T_{Min}), in response to a step-type reference power profile.

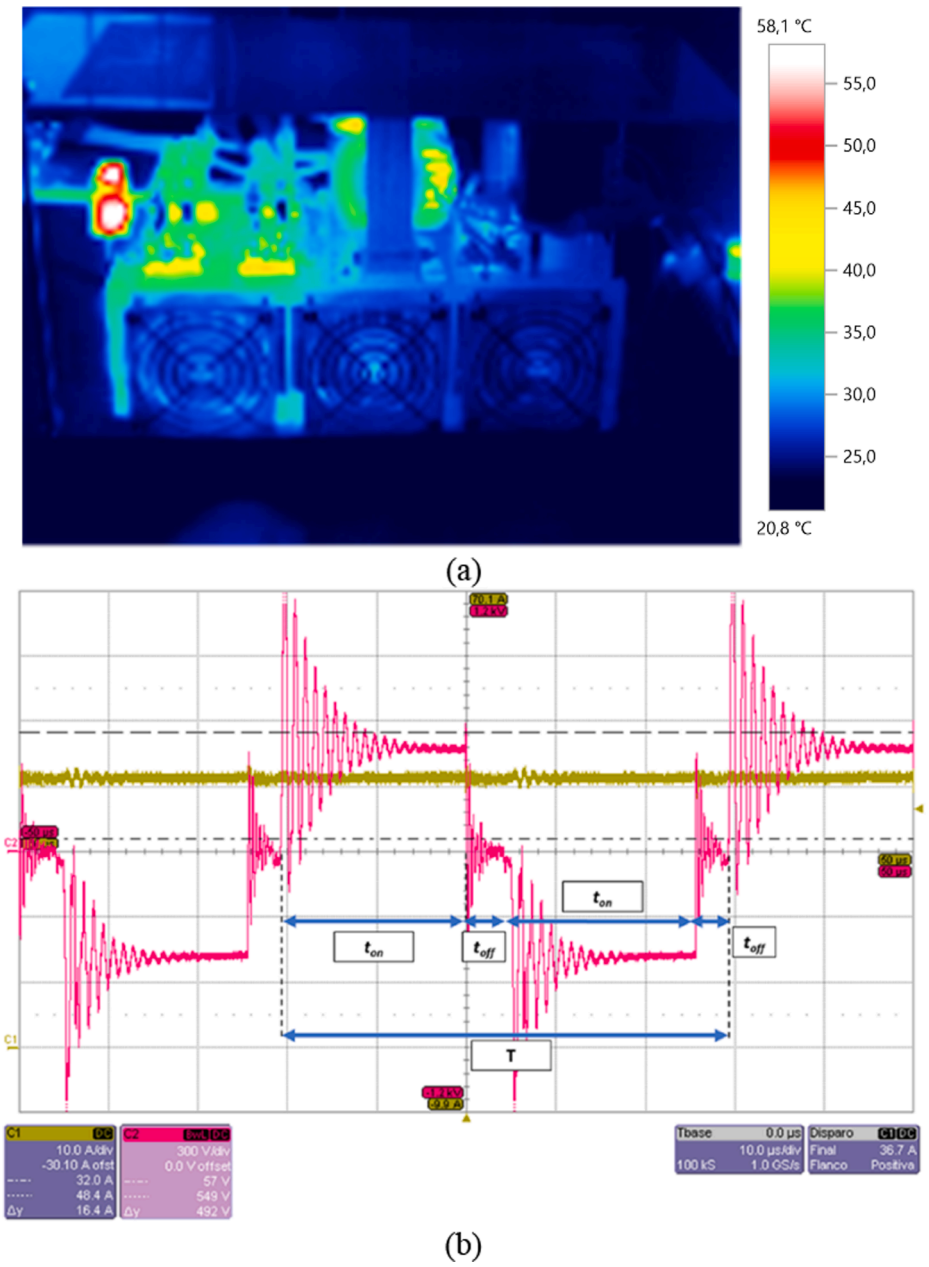

Fig. 20. (a) Thermography of the developed DC/DC push–pull converter; (b) FC output current (ochre line, channel C1(x, y): 10.0 µs/div, 10.0 A/div); voltage waveform on secondary winding of the DC/DC transformer (fuchsia line, channel C2 (x, y): 10.0 µs/div, 300 V/div).

cycles are very low and insufficient currents are generated in the converter to operate efficiently), the efficiency of the converter exceeds 90%, which is an excellent result but, in addition, as the stack will usually operate at its rated power, efficiency will be even better, above 93–94%.

Fig. 21 shows an atypical behavior for the $V_i = 60$ V curve. The explanation is the following. The measurements for the efficiency curves of the DC/DC converter were performed with its own data acquisition electronics. The CU (ATmega2560 microcontroller, see Fig. 9) has 10-bit resolution for analog inputs. The current measuring channel has been designed to measure a maximum current of 70 A, so the quantization error is of 70/1024 = 0.068 A. Thus, theoretically, the current measurement channel would be capable of measuring a current as small as 0.068 A. Of course, this would be the case if the voltage source at the input of the converter were a laboratory source. However, the voltage source at the input of the converter is the output of the FC (see Fig. 20 (b)), which causes a major problem in the measurements due to noise. This is present on the analog input of the microcontroller. Therefore, for low current values, the superimposed noise masks the true value of the signal. This explains the curves in Fig. 21 where the behaviour for $V_{in} =$ 40 V and 50 V is as expected (considering nonlinearities of course). However, not for $V_{in} = 60$ V, because at 20% of rated power the current is very low. Only when the power starts to increase and, therefore, the current, the behaviour of the $V_{in} = 60$ V curve is as expected. This limitation of the measurement system is not a problem in practice, since it has been designed to work at its rated power where, as can be seen in Fig. 20(b), the ripple is only 3% of the signal.

Finally, based on the results and its discussion, the correct design and sizing of the complete MSFCS and the VI that controls and monitors it is validated.

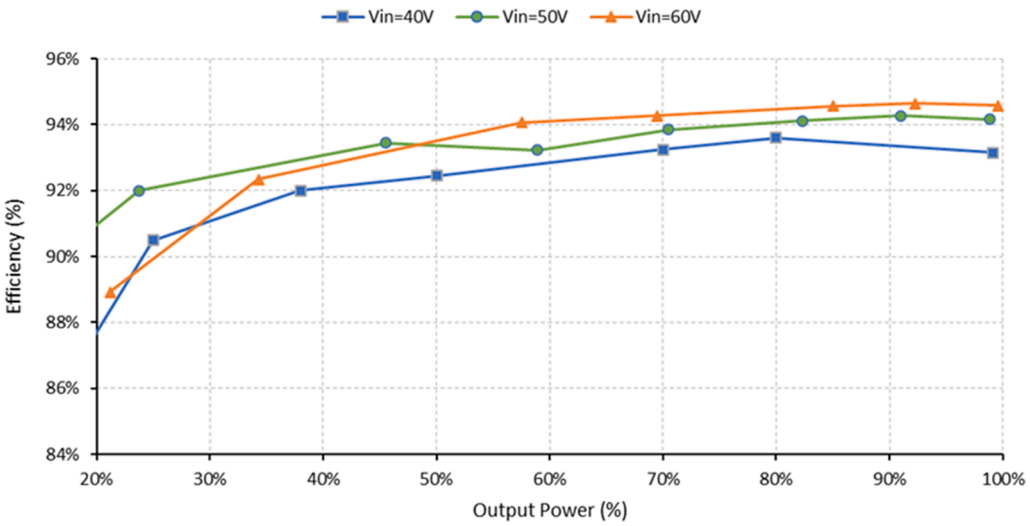

Fig. 21. Efficiency curves of the developed DC/DC converter.

5. Conclusions

In recent years there has been a clear commitment to research in renewable microgrids, especially those based on hydrogen as an energy vector. However, due to the still high cost of hydrogen technologies and the often lack of commercial solutions, there are currently few examples of renewable hydrogen systems integrated and operational in real renewable microgrids. The FC, the most expensive and sensitive element of the microgrid (also, although to a lesser extent, the electrolyzer if the hydrogen is produced in the microgrid itself), plays a fundamental role. For integration, MSFCS-based solutions built with ACFCs provide, at lower cost, greater flexibility, robustness and resilience to the hydrogen system, also allowing to adapt the power to that required in the microgrid.

The correct operation of the AC-MSFCS requires indispensable auxiliary elements, such as the BoP, the power converter, the monitoring and acquisition electronics and, for its optimal operation, it also requires a correct management of its degradation, so that all the stacks always have a similar degree of deterioration. This leads to the design of complex EMSs, as they must handle many parameters, control loops and information. Comprehensive solutions, such as the one shown in this article, are required to easily connect an AC-MSFCS in a microgrid, as a black box with two terminals: hydrogen as input and regulated power/voltage as output. In this respect, only partial solutions have been found in the scientific literature.

This paper presents in a practical way, with proven results, a comprehensive, scalable and replicable turnkey solution, which allows the integration and management of a AC-MSFCS in a real renewable microgrid supported by a HVDC bus. The design methodology developed allows to easily carry out as many FC lines as needed, depending on the power required by the AC-MSFCS, which allows its scalability, since all the lines are identical. For this purpose, all the elements that make up the AC-MSFCS have been developed step by step, i.e. the BoP of each stack and its DC/DC power converter, as well as the acquisition and monitoring electronics for its management, control and quantification of degradation. Monitoring and control of the AC-MSFCS has been solved through the development of local control loops, a centralized CU and a VI that provides a bidirectional connection to the EMS, as well as through a user-friendly interface to ergonomically operate the AC-MSFCS. Thanks to the available information and local control loops, the EMS can implement advanced strategies that increase the efficiency of the AC-MSFCS, as well as its lifespan, making uniform use of its stacks and, consequently, balancing their inevitable deteriorations.

Experimental results obtained with the developed AC-MSFCS, connected to a HVDC bus supported by batteries, validated the excellent performance of the proposed solution. All necessary AC-MSFCS parameters were measured and processed correctly by the EMS, implementing the required control actions and alarm monitoring. In particular, the temperature control loop developed made it possible to keep the stack temperature within safe operating limits whatever the power output. On the other hand, the developed power control loop allowed the injection of the power setpoint provided by the EMS, through the developed VI, to the DC bus; for this purpose, a push–pull topology power converter has been developed, which has shown an average efficiency higher than 90% together with an excellent thermal performance. Finally, as a further performance of the development, the cumulative degradation of the stack was quantified, with maximum values closed at 10 V with respect to the curve at its BoL, and up to 475 mV at the cell level.

As for the limitations of the designed AC-MSFCS, for practical purposes it does not have any, because each line of stacks works independently, so that, in the event of a deterioration or malfunction of a line, its elements can be replaced or repaired with the rest of the lines working. Moreover, according to the design methodology shown step by step in the article, the AC-MSFCS elements could be reconfigured, according to power, output voltage and/or control requirements.

Future work focuses on the direct application of the developments shown for the design of a AC-MSFCS with 10 brand new stacks to increase the hydrogen power of the microgrid in Fig. 1 to >30 kW. The microgrid is connected to the Campus grid, so it will provide the opportunity to know in real time, on a practical microgrid, the deterioration of the stacks (it can be quantified) as well as the balance that the EMS will be doing to achieve a similar continuous deterioration in all the stacks. This will make it possible to study the cause-effect relationships between operating conditions and fuel cell degradation, which will enable new lines of EMS research to be launched to increase the efficiency and lifespan of these systems, as well as to improve power sharing in the microgrid.

Declaration of Competing Interest

The authors declare that they have no known competing financial interests or personal relationships that could have appeared to influence the work reported in this paper.

Acknowledgements

This research was funded by "H2Integration&Control. Integration and Control of a hydrogen-based pilot plant in residential applications for energy supply" Spanish Government, grant Ref: PID2020-116616RB-C31,"; and "SALTES: Smartgrid with reconfigurable Architecture for testing controL Techniques and Energy Storage priority" by Andalusian Regional Program of R+D+, grant Ref: P20-00730.

References

[1] Chaudhry SM, Ahmed R, Shafiullah M, Duc Huynh TL. The impact of carbon emissions on country risk: evidence from the G7 economies. J Environ Manage 2020;265:110533.
[2] Vivas FJ, De las Heras A, Segura F, Andújar JM. A review of energy management strategies for renewable hybrid energy systems with hydrogen backup. Renew Sustain Energy Rev 2018;82:126–55.
[3] Ferrario AM, Vivas FJ, Manzano FS, Andújar JM, Bocci E, Martirano L. Hydrogen vs. battery in the long-term operation. A comparative between energy management strategies for hybrid renewable microgrids. Electronics (Switzerland) 2020;9:1–28. https://doi.org/10.3390/electronics9040698.
[4] Petrollese M, Valverde L, Cocco D, Cau G, Guerra J. Real-time integration of optimal generation scheduling with MPC for the energy management of a renewable hydrogen-based microgrid. Appl Energy 2016;166:96–106. https://doi.org/10.1016/j.apenergy.2016.01.014.
[5] İnci M. A flexible perturb & observe MPPT method to prevent surplus energy for grid-failure conditions of fuel cells. Int J Hydrogen Energy 2021;46:39483–98. https://doi.org/10.1016/j.ijhydene.2021.09.185.
[6] İnci M, Aygen MS. A modified energy management scheme to support phase balancing in grid interfaced photovoltaic/fuel cell system. Ain Shams Eng J 2021;12:2809–22. https://doi.org/10.1016/j.asej.2020.12.018.
[7] Lin R-H, Xi X-N, Wang P-N, Wu B-D, Tian S-M. Review on hydrogen fuel cell condition monitoring and prediction methods. Int J Hydrogen Energy 2019;44(11):5488–98.
[8] Zhang Y, Wei W. Decentralized coordination control of PV generators, storage battery, hydrogen production unit and fuel cell in islanded DC microgrid. Int J Hydrogen Energy 2020;45:8243–56. https://doi.org/10.1016/j.ijhydene.2020.01.058.
[9] Pu Y, Li Q, Chen W, Liu H. Hierarchical energy management control for islanding DC microgrid with electric-hydrogen hybrid storage system. Int J Hydrogen Energy 2019;4:5153–61. https://doi.org/10.1016/j.ijhydene.2018.10.043.
[10] Alam M, Kumar K, Dutta V. Droop based control strategy for balancing the level of hydrogen storage in direct current microgrid application, Journal of Energy Storage. (2020) 102106. https://doi.org/10.1016/j.est.2020.102106.
[11] Alam M, Kumar K, Verma S, Dutta V. Renewable sources based DC microgrid using hydrogen energy storage: modelling and experimental analysis. Sustain Energy Technol Assess 2020;42:100840. https://doi.org/10.1016/j.seta.2020.100840.
[12] Vivas FJ, De Las Heras A, Segura F, Andujar JM. Configuration of a Fuel Cell system. Clues to choose between a modular or single stack-based design, in. IECON Proc (Industrial Electronics Conference) 2016. https://doi.org/10.1109/IECON.2016.7793574.
[13] Calderón AJ, Vivas FJ, Segura F, Andújar JM. Integration of a multi-stack fuel cell system in microgrids: a solution based on model predictive control. Energies 2020;13(18):4924.
[14] Bahrami M, Martin J-P, Maranzana G, Pierfederici S, Weber M, Meibody-Tabar F, et al. Multi-stack lifetime improvement through adapted power electronic architecture in a fuel cell hybrid system. Mathematics 2020;8:739. https://doi.org/10.3390/math8050739.
[15] De las Heras A, Vivas FJ, Segura F, Redondo MJ, Andújar JM. Air-cooled fuel cells: Keys to design and build the oxidant/cooling system. Renew Energy 2018;125:1–20.
[16] Segura F, Andújar JM, Durán E. Analog current control techniques for power control in PEM fuel-cell hybrid systems: a critical review and a practical application. IEEE Trans Ind Electron 2011;58:1171–84. https://doi.org/10.1109/TIE.2010.2049710.
[17] Segura F, Andújar JM. Modular PEM fuel cell SCADA & simulator system. Resources 2015;4:692–712. https://doi.org/10.3390/resources4030692.
[18] Sarmiento-Carnevali M, Serra M, Batlle C. Distributed parameter model simulation tool for PEM fuel cells. Int J Hydrogen Energy 2014;39:4044–52. https://doi.org/10.1016/j.ijhydene.2013.04.015.
[19] Vivas FJ, Heras AdL, Segura F, Andújar JM. Cell voltage monitoring All-in-One. A new low cost solution to perform degradation analysis on air-cooled polymer electrolyte fuel cells. Int J Hydrogen Energy 2019;44(25):12842–56.
[20] Mehida H, Ayad MY, Saadi R, Kraa O, Aboubou A. Multi-Stack Fuel Cells and Interleaved DC/DC Converters Interactions for Embedded Applications. In: Proceedings of 2018 3rd International Conference on Electrical Sciences and Technologies in Maghreb; 2018. (2019). p. 1–6. https://doi.org/10.1109/CISTEM.2018.8613600.
[21] Frappé E, De Bernardinis A, Bethoux O, Ieee M, Marchand C. Corrective action with power converter for faulty multiple fuel cells generator used in transportation Emmanuel. IEEE Vehicle Power Propul Conf 2010:1–6.
[22] Yan Y, Li Q, Chen W, Huang W, Liu J, Liu J. Online Control & Power Coordination Method for Multi-stack Fuel Cells System Based on Optimal Power Allocation, IEEE Transactions on Industrial Electronics. 0046 (2020) 1–1. https://doi.org/10.1109/tie.2020.3016240.
[23] Fernandez AMI, Kandidayeni M, Boulon L, Chaoui H. An adaptive state machine based energy management strategy for a multi-stack fuel cell hybrid electric vehicle. IEEE Trans Veh Technol 2020;69:220–34. https://doi.org/10.1109/TVT.2019.2950558.
[24] Marx N, Cardozo J, Boulon L, Gustin F, Hissel D, Agbossou K. Comparison of the series and parallel architectures for hybrid multi-stack fuel cell - battery systems. In: 2015 IEEE Vehicle Power and Propulsion Conference, VPPC 2015 – Proceedings; 2015. p. 2–7. https://doi.org/10.1109/VPPC.2015.7352915.
[25] Kolli A, De-Bernardinis A, Khatir Z, Gaillard A, Bethoux O, Hissel D. Part-load control stategy of a 20kW SiC power converter for embedded PEMFC multi-stack architectures. In: IECON 2015–41st Annual Conference of the IEEE Industrial Electronics Society; 2015. p. 4627–32. https://doi.org/10.1109/IECON.2015.7392821.
[26] Depature C, Boulon L, Sicard P, Fournier M. Simulation model of a multi-stack fuel cell system. In: 2013 15th European Conference on Power Electronics and Applications, EPE 2013; 2013. https://doi.org/10.1109/EPE.2013.6634727.
[27] Valdez-resendiz JE, Sanchez VM, Rosas-caro JC, Mayo-maldonado JC, Sierra JM, Barbosa R. Continuous input-current buck-boost DC-DC converter for PEM fuel cell applications. Int J Hydrogen Energy 2017;42:30389–99. https://doi.org/10.1016/j.ijhydene.2017.10.077.
[28] Lai CM, Yang MJ. A high-gain three-port power converter with fuel cell, battery sources and stacked output for hybrid electric vehicles and DC-microgrids. Energies 2016;9:6–9. https://doi.org/10.3390/en9030180.
[29] Wu Y, Huangfu Y, Ma R, Ravey A, Chrenko D. A strong robust DC-DC converter of all-digital high-order sliding mode control for fuel cell power applications. J Power Sources 2019;413:222–32. https://doi.org/10.1016/j.jpowsour.2018.12.049.
[30] Somaiah B, Agarwal V, Choudhury SR, Duttagupta SP, Govindan K. Analysis and comparative study of pulsating current of fuel cells by inverter load with different power converter topologies. Int J Hydrogen Energy 2011;36:15018–28. https://doi.org/10.1016/j.ijhydene.2011.04.118.
[31] Delshad M, Farzanehfard H. A new soft switched push pull current fed converter for fuel cell applications. Energy Convers Manage 2011;52:917–23. https://doi.org/10.1016/j.enconman.2010.08.019.
[32] Farhani S, Barhoumi EM, Bacha F. Design and hardware investigation of a new configuration of an isolated DC-DC converter for fuel cell vehicle. Ain Shams Eng J 2021;12(1):591–8.
[33] Elangovan D, Saravanakumar R, Nigam S. Design and implementation of soft switched high gain current fed full bridge DC-DC converter for fuel cell applications. Energy Procedia 2014;54:246–59. https://doi.org/10.1016/j.egypro.2014.07.268.
[34] Al-saffar MA, Ismail EH. A high voltage ratio and low stress DC-DC converter with reduced input current ripple for fuel cell source. Renew Energy 2015;82:35–43. https://doi.org/10.1016/j.renene.2014.08.020.
[35] Bhaskar MS, Padmanaban S, Holm-Nielsen JB. Double stage double output DC-DC converters for high voltage loads in fuel cell vehicles. Energies 2019;12(19):3681.
[36] Pecen R, Yildiz F, Baltaci K. Design and implementation of a hydrogen fuel cell data acquisition and monitoring scheme for educational institutions. ASEE Annual Conference and Exposition, Conference Proceedings 2008. https://doi.org/10.18260/1-2–3672.
[37] Zhou S, Yu H, Chen F. A monitor system based on virtual instrument for fuel cell commuter. In: 2011 International Conference on Electric Information and Control Engineering; 2011. p. 3869–71. https://doi.org/10.1109/ICEICE.2011.5777042.
[38] Zeng J, Luo J, Xie W. Solutions of fuel cell measurement & control system based on virtual instrument technology. Appl Mech Mater 2012;143–144:386–90. https://doi.org/10.4028/www.scientific.net/AMM.143-144.386.
[39] Andújar JM, Segura F, Isorna F, Calderón AJ. Comprehensive diagnosis methodology for faults detection and identification, and performance improvement of air-cooled polymer electrolyte fuel cells. Renew Sustain Energy Rev 2018;88:193–207.
[40] Vivas FJ, Segura F, de las Heras A, Andujar JM. System for monitoring and controlling fuel cells, publication Number WO/2019/102053. https://patentscope.wipo.int/search/es/detail.jsf?docId=WO2019102053, n.d.
[41] Andujar Marquez JM, Segura Manzano F. Patent: System for generating electric power. Publication Number WO/2015/169979. https://patentscope.wipo.int/search/en/detail.jsf?docId=WO2015169979&tab=PCTBIBLIO, (n.d.). https://doi.org/10.1016/j.jpowsour.2008.08.059.
[42] Calderón AJ, González I, Calderón M, Segura F, Andújar JM. A new, scalable and low cost multi-channel monitoring system for polymer electrolyte fuel cells. Sensors (Switzerland) 2016;16:1–19. https://doi.org/10.3390/s16030349.
[43] BALLARD, FCgen ® -1020ACS Fuel Cell Stack Product Manual and Integration Guide; 2011.
[44] Chen H, Pei P, Song M. Lifetime prediction and the economic lifetime of proton exchange membrane fuel cells. Appl Energy 2015;142:154–63. https://doi.org/10.1016/j.apenergy.2014.12.062.

[45] Fernández RÁ, Cilleruelo FB, Martínez IV. A new approach to battery powered electric vehicles: A hydrogen fuel-cell-based range extender system. Int J Hydrogen Energy 41 (2016) 4808–4819. https://doi.org/https://doi.org/10.1016/j.ijhydene.2016.01.035.
[46] Corrêa JM, Farret FA, Canha LN, Simoes MG. An electrochemical-based fuel-cell model suitable for electrical engineering automation approach. IEEE Trans Ind Electron 2004;51:1103–12. https://doi.org/10.1109/TIE.2004.834972.
[47] Oh H, Lee WY, Won J, Kim M, Choi YY, Bin Han S. Residual-based fault diagnosis for thermal management systems of proton exchange membrane fuel cells. Appl Energy. 277 (2020) 115568. https://doi.org/10.1016/j.apenergy.2020.115568.
[48] Trujillo CL, Velasco D, Figueres E, Garcerá G, Ortega R. Modeling and control of a push-pull converter for photovoltaic microinverters operating in island mode. Appl Energy 2011;88:2824–34. https://doi.org/10.1016/j.apenergy.2011.01.053.
[49] Yan F, Li J, Du C, Zhao C, Zhang W, Zhang Y. A coupled-inductor DC-DC converter with input current ripple minimization for fuel cell vehicles. Energies 2019;12(9):1689.
[50] Dixon Jr LH. Magnetics Design Handbook. Texas Instruments 2002.
[51] Wu S, Sun A, Xu W, Zhang Q, Zhai F, Logan P, et al. Iron-based soft magnetic composites with Mn-Zn ferrite nanoparticles coating obtained by sol-gel method. J Magn Magn Mater 2012;324:3899–905. https://doi.org/10.1016/j.jmmm.2012.06.042.
[52] Abo-Elyousr FK, Guerrero JM, Ramadan HS. Prospective hydrogen-based microgrid systems for optimal leverage via metaheuristic approaches. Appl Energy 2021;300:117384. https://doi.org/10.1016/j.apenergy.2021.117384.